

## Chapter 4

**$\mu$ -Alkoxo bridged dicopper (II)  
complexes of compartmental Schiff  
bases of bidentate aldehydes &  
naphthonimines**

---

---

**Chapter 4:  $\mu$ -alkoxo bridged dicopper(II) complexes of compartmental Schiff Bases of aldehydes and naphthonimines**

4.1 INTRODUCTION	207
4.2 EXPERIMENTAL SECTION	209
4.2.1 Materials and Methods	209
4.2.2 Synthesis of the Schiff base ligand (L <sup>9</sup> -L <sup>12</sup> )	209
4.2.3 Synthesis of the binuclear copper complexes (C9-C12)	210
4.2.4 SOD mimic activity	211
4.2.5 Ascorbic Acid Oxidase (AAO) activity	211
4.2.6 Catecholase activity	212
4.2.5 Physical Measurements	214
4.2.5.1 Infrared studies	214
4.2.5.2 NMR studies	214
4.2.5.3 Mass studies	214
4.2.5.4 Electronic studies	214
4.2.5.5 Photoluminescence studies	214
4.2.5.6 Elemental Analysis	214
4.2.5.7 ESR studies	214
4.2.5.8 Magnetic studies	215
4.2.5.9 Single Crystal X-ray Diffraction	215
4.2.5.10 Molecular Modelling	215
4.3 RESULTS AND DISCUSSION	215
4.3.1 Characterization of ligands	215
4.3.1.1 IR spectra	215
4.3.1.2 NMR Spectra	216
4.3.1.3 Electronic spectra	216

---

4.3.1.4 Photoluminescence spectra	217
4.3.1.5. Mass Spectra	217
4.3.2 Characterization of complexes	217
4.3.2.1 Elemental analysis	217
4.3.2.2 IR spectra	218
4.3.2.3 Mass spectra	218
4.3.2.4 Electronic spectra	219
4.3.2.5 Photoluminescence spectra	220
4.3.2.6 Crystal structure of complex <b>C9</b>	221
4.3.2.7 ESR spectra	224
4.3.2.8 Magnetic studies	225
4.3.2.9 Quantum chemical calculations	226
4.3.3 SOD mimic activity	231
4.3.4 Ascorbic Acid Oxidase (AAO) activity	233
4.3.5 Catecholase activity	239
4.4 CONCLUSION	244
Supplementary Information	245
References	263

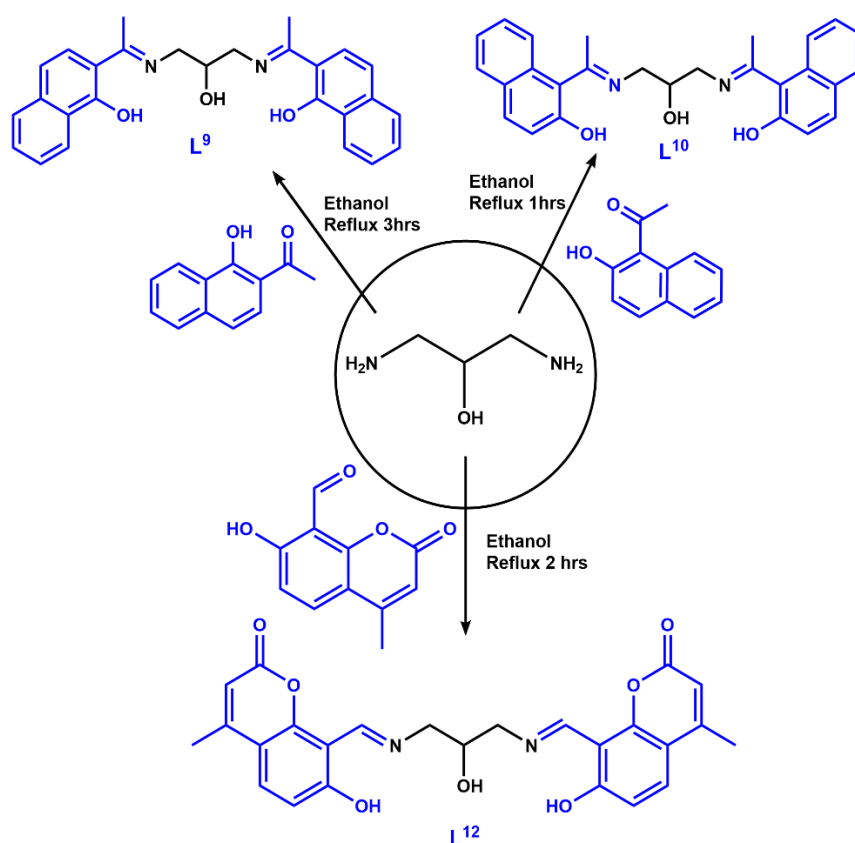
## 4.1 INTRODUCTION

The  $\mu$ -alkoxo bridged copper(II) complexes have attracted attention as model compounds for the active sites of various type 3 copper proteins.<sup>1,2</sup> Various copper(II) complexes have been synthesized and well characterized to mimic these sites. There are reports based on electrochemical<sup>3</sup> and mechanistic and pH-based studies on the model binuclear complexes in the literature.<sup>2</sup> Magnetic properties of such models compounds can be varied by two different diamagnetic bridges between two copper(II) ions in close proximity making it either ferromagnetic or weakly antiferromagnetic or strongly antiferromagnetic coupled complexes.<sup>1,4</sup> Due to the proximity of two metal ions and electron delocalization between them, the binuclear copper(II) complexes are emerging as good candidates for developing bioactive molecules and bioinspired catalysts for various oxidation reactions. Gentshev *et al*<sup>5</sup> synthesized a novel dicopper(II) complex with  $N_2O_3$  donor ligand N,N,N',N'-bis[(2-hydroxybenzyl)(N-methylimidazolyl)]-2-ol-1,3-propanediamine (Hbhmipo) with copper(II) perchlorate and sodium acetate in acetonitrile/ethanol medium. The crystal structure, magnetic properties and its catecholase activity have been reported.<sup>5</sup> Kulkarni *et al*<sup>6</sup> have synthesized a series of Co(II), Ni(II) and Cu(II) complexes with Schiff bases derived from 8-formyl-7-hydroxy-4-methyl coumarin and o-chloroaniline/o-toluidine. These complexes were screened for their antibacterial and antifungal activities by MIC method.<sup>6</sup> Nagesh *et al*<sup>3</sup> synthesized new octahedral [Cu(L)(H<sub>2</sub>O)<sub>2</sub>], [Co(L)<sub>2</sub>], [Ni(L)<sub>2</sub>] and [Zn(L)(Cl)(H<sub>2</sub>O)<sub>2</sub>] complexes with ONO donor Schiff base ligand 2-((7-hydroxy-4-methyl-2-oxo-2H-chromen-8-yl)methylene)-N-(4-phenylthiazol-2-yl)hydrazinecarboxamide (L). The antimicrobial activity of all complexes was found to be enhanced due to the presence of the metal ion. DNA cleavage studies revealed that they have good cytotoxic property and ability to cleave pBR322 DNA. Halli *et al*<sup>7</sup> synthesized metal complexes of the type ML<sub>2</sub>, where M = Co(II), Ni(II), Cu(II), Zn(II), Cd(II), Hg(II) and L = Schiff's base derived from the condensation of naphthofuran-2-carbohydrazide with 8-formyl-7-hydroxy-4-methyl coumarin and studied DNA cleavage, antioxidant activities and *in vitro* antibacterial and antifungal activities.<sup>7</sup>

Looking at the varied biological activity of chromene and their Schiff bases, it was thought of interest to combine them in dicopper complex form and examine their efficacy towards oxidation of substrates, radical quenching and evaluate their biological activity. Also, it was of interest to study the effect of structural changes in the ligands

on the activity of dicopper(II) complexes. Hence, the work described in this chapter was focussed on the complexes of binucleating ligands derived from a chromene and two isomeric naphthones.

In the present work, binucleating Schiff bases were formed by condensation of 1,3-diamino-2-propanol with two isomeric hydroxyacetone naphthones and 8-formyl-7-hydroxy-4-methyl coumarin. Binucleating moieties have two ONO binding sites with a bridging alkoxo group along with phenoxo oxygen and imine nitrogen atoms.



**Scheme 4.1.1** Schematic representation of synthesized ligands  $L^9$ ,  $L^{10}$  and  $L^{12}$

Herein, we report the synthesis and characterization of three binucleating copper(II)- $\mu$ -alkoxo- $\mu$ -acetate bridged complexes (*viz.*  $[\text{Cu}_2(L_9)(\text{OAc})] \cdot \text{H}_2\text{O}$  (**C9**),  $[\text{Cu}_2(L_{10})(\text{OAc})] \cdot 3\text{H}_2\text{O}$  (**C10**) and  $[\text{Cu}_2(L_{12})(\text{OAc})]$  (**C12**)) of Schiff bases ( $L^9$ ,  $L^{10}$  and  $L^{12}$ ) (**Scheme 4.1.1**) which acts as structural and functional models for the active site of catechol oxidase.

The catecholase and ascorbate acid oxidase activity of these complexes have been studied by using appropriate substrates and compared with known catecholase mimics. Quantum chemical parameters at density functional theory (DFT) level have been used

to get insight into the electronic and molecular structures of these complexes. These complexes have also been explored for SOD mimetic activity. The results of these investigations have been discussed in this chapter.

## 4.2 EXPERIMENTAL SECTION

### 4.2.1 Materials and Methods

Copper acetate monohydrate, hexamine has been procured from Merck. 1,3-diamino-2-propanol, 1-hydroxy acetonephthone, 2-hydroxy acetonephthone, 3,5-DTBC, 4-methyl catechol, dopamine, pyrocatechol, 2,3-dihydroxy naphthalene have been purchased from Sigma Aldrich and used as received. Potassium iodide and ammonium molybdate has been purchased from Loba Chem. Diethyl ether,  $\beta$ -NADH, phenazine methosulphate (PMS), nitroblue tetrazolium (NBT), acetic acid, sodium dihydrogen phosphate monohydrate and sodium phosphate dibasic anhydrous, 8-hydroxy-4-methylcoumarin has been procured from SRL chemicals. 7-formyl-8-hydroxy-4-methylcoumarin has been prepared using literature method.<sup>6</sup> Methanol and dimethyl sulfoxide has been procured from Spectrochem. All other chemicals used were of AR grade and were used as received. For spectroscopic studies, spectroscopic grade solvent was used. The solvents have been distilled prior to use and dried according to standard procedure wherever necessary.

### 4.2.2 Synthesis of the Schiff base ligand ( $L^9$ - $L^{12}$ )

Ligand  $L^9$ : A hot ethanolic solution (10mL) of 1-hydroxy acetonephthone (0.186g, 1 mmol) was added dropwise to a 5mL hot ethanolic solution of 1,3-diaminopropan-2-ol (0.045g, 0.5mmol) in a RB flask. The mixture was allowed to reflux for 3 hours by monitoring the reaction with the help of TLC. At the end of 3 hours, a single spot for the product appeared on TLC. Within few hours, fluorescent yellow microcrystalline solid started precipitating. The reaction mixture was concentrated to about 10 ml and cooled to obtain fluorescent yellow microcrystalline solid. The product was filtered and washed with cold ethanol to remove the traces of any soluble impurities and unreacted reactants. No further purification was required as single spot was obtained on TLC. Yield = 0.105g (49.29%). Solubility: CH<sub>3</sub>OH: MDC (1:1), DMSO. M.P.: 256-258°C

Ligand  $L^{10}$ : (10 mL) of a hot ethanolic solution of 2-hydroxy acetonephthone (0.372g, 2 mmol) was added dropwise to a 5 mL hot ethanolic solution of 1,3-diaminopropan-2-ol (0.090g, 1 mmol) in a RB flask. The mixture was allowed to reflux for 1 hours by

monitoring the reaction with the help of TLC. At the end of 1 hours, a single spot for the product appeared on TLC. The reaction mixture was concentrated to about 10 ml and cooled to obtain yellow-orange microcrystalline solid. The product was filtered and washed with cold ethanol to remove the traces of any soluble impurities and unreacted reactants. No further purification was required as single spot was obtained on TLC. Yield = 0.227g (53.29%). Solubility: CH<sub>3</sub>OH, DMSO. M.P.: 72-74°C

Ligand **L<sup>11</sup>**: (10 mL) of a hot ethanolic solution of 4-methyl thiophene-2-carbaldehyde (0.252g, 2 mmol) was added dropwise to a 5 mL hot ethanolic solution of 1,3-diaminopropan-2-ol (0.090g, 1 mmol) in a RB flask. The mixture was allowed to reflux for 1 hours by monitoring the reaction with the help of TLC. At the end of 1 hours, a single spot for the product appeared on TLC. This ligand was not isolated and was used as it is for complex preparation.

Ligand **L<sup>12</sup>**: A 10 mL hot ethanolic solution of 7-formyl-8-hydroxy-4-methylcoumarin (0.204g, 1 mmol) was added dropwise to a 5 mL hot ethanolic solution of 1,3-diaminopropan-2-ol (0.0451g, 0.5mmol) in a RB flask. The mixture was allowed to reflux for 45 mins and the reaction was monitored with the help of TLC. At the end of 45 mins, a single spot for the product appeared on TLC. Within few hours, yellow colour microcrystalline solid started precipitating from the solution. The reaction mixture was concentrated to about 10 ml and cooled to obtain yellow microcrystalline solid. The product was filtered and washed with cold ethanol to remove the traces of any soluble impurities and unreacted reactants. No further purification was required as single spot was obtained on TLC. Yield = 0.180g (77.82%). Solubility: DMF, DMSO (partially soluble). M.P.: 262°C (decomp. black).

The purity of all ligands was checked by TLC.

#### ***4.2.3 Synthesis of the binuclear copper complexes (C9-C12)***

Complex **C9** ([Cu<sub>2</sub>(L<sup>9</sup>)(OAc)]·H<sub>2</sub>O): A 15 mL hot ethanolic solution of 1-hydroxy acetophenone (0.8383g, 4.5 mmol) was added dropwise to 10 mL of hot ethanolic solution of 1,3-diaminopropan-2-ol (0.195g, 2.25 mmol) in a RB flask. The mixture was allowed to reflux for 3 hours. A hot ethanolic solution, (15 mL), of Cu(OAc)<sub>2</sub>·H<sub>2</sub>O (0.8612g, 4.5mmol) was added to the ligand solution and the resulting solution was allowed to reflux for 2 hrs. A dark green colour microcrystalline solid precipitated out within few hours of reaction. the solid was filtered and washed several times (10 x 2mL)

with cold ethanol to remove the traces of any starting compounds. Single crystal for X-ray diffraction was obtained by recrystallization of the complex from dichloromethane. Yield: 0.995g (36.79%). Solubility: Chloroform, Dichloromethane, DMSO, DMF.

Complex **C10** ( $[\text{Cu}_2(\text{L}^{10})(\text{OAc})]\cdot 3\text{H}_2\text{O}$ ): A 15 mL hot ethanolic solution of 2-hydroxy acetophenone (0.744g, 2 mmol) was added dropwise to a 10 mL hot ethanolic solution of 1,3-diaminopropan-2-ol (0.180g, 1mmol) in a RB flask. The mixture was allowed to reflux for 3 hours. A hot solution of  $\text{Cu}(\text{OAc})_2\cdot\text{H}_2\text{O}$  (0.796g, 2mmol) in 15 mL ethanol was added to ligand solution and the resulting solution was allowed to reflux for 2 hrs. A dark green colour microcrystalline solid precipitated out within few hours of the reaction. The solid was filtered and washed several times, (10 x 2 mL), with cold ethanol to remove the traces of any unreacted amine and acetophenone. Yield: 0.799g (43.28%). Solubility: Methanol, DMSO, DMF.

Complex **C11**: Repeated attempts to synthesize **L<sup>11</sup>** and **C11** were unsuccessful. Hence, this complex was not studied further.

Complex **C12** ( $[\text{Cu}_2(\text{L}^{12})(\text{OAc})]$ ): A 15 mL hot ethanolic solution of 8-formyl-7-hydroxy-4-methyl coumarin (0.204g, 1 mmol) was added dropwise to a 10 mL hot ethanolic solution of 1,3-diaminopropan-2-ol (0.045g, 0.5mmol) in a RB flask. The mixture was allowed to reflux for 45 mins. A hot solution of  $\text{Cu}(\text{OAc})_2\cdot\text{H}_2\text{O}$  (0.200g, 1mmol) in 15 mL ethanol was added to ligand solution and the resulting solution was allowed to reflux for 2 hrs. A dark green colour microcrystalline solid precipitated out within few hours of reaction. the product was filtered and washed several times, (10 x 2 mL), with cold ethanol to remove the traces of any amine and aldehyde. Yield: 0.246g (37.96%). Solubility: Methanol, DMSO, DMF.

#### 4.2.4 SOD mimic activity

The superoxide dismutase (SOD) activity was measured using a non-enzymatic method (NADH-PMS-NBT assay) (**Scheme 2.2.4.1**)<sup>8-11</sup> as explained in **section 2.2.4** of chapter 2.

#### 4.2.5 Ascorbic Acid Oxidase (AAO) activity

Ascorbic Acid Oxidase (AAO) activity of all synthesized complexes has been evaluated by kinetic studies with ascorbic acid as substrate wherein three different parameters such as substrate concentration, catalyst concentration and temperature have been

varied. The concentration and temperature employed for this activity are mentioned below in a tabular form (**Table 4.2.5.1**).

**Table 4.2.5.1** Concentration of ascorbic acid and catalyst with different parameters employed in this study

Parameters	Concentration(mM)/Temp (°C)						
<b>C9</b>							
Substrate	[Cat=0.004mM and Temp= 30°C]						
	0.16	0.14	0.12	0.10	0.08	0.06	0.04
Catalyst	[Sub=0.1mM and Temp= 30°C]						
	0.002	0.003	0.004	0.005	0.006		
Temperature	[Sub=0.004mM and Cat=0.004mM]						
	30	35	40	45	50		
<b>C10</b>							
Substrate	[Cat=0.004mM and Temp= 30°C]						
	0.02	0.04	0.06	0.08	0.1	0.12	
Catalyst	[Sub=0.1mM and Temp= 30°C]						
	0.002	0.003	0.004	0.005	0.006		
Temperature	[Sub=0.1mM and Cat=0.004mM]						
	30	35	40	45	50		
<b>C12</b>							
Substrate	[Cat=0.004mM and Temp= 30°C]						
	0.12	0.10	0.08	0.06	0.04	0.02	
Catalyst	[Sub=0.004mM and Temp= 30°C]						
	0.002	0.004	0.006	0.008	0.01		
Temperature	[Sub=0.004mM and Cat=0.004mM]						
	30	35	40	45			

The reaction rates, order and activation energy of reactions were calculated as explained in **section 2.2.4** in chapter 2. The ascorbate oxidase activity of all five complexes was studied by treating  $1 \times 10^{-6}$  M complex solution with  $1 \times 10^{-4}$  M ascorbic acid solution under aerobic condition at 30°C. The time dependent wavelength scan was performed in acetate buffer medium (pH 5.5) to understand the potential of all complexes as catalyst towards the oxidation of ascorbic acid. The kinetic studies of the oxidation of ascorbic acid of all complexes were performed and the rates were determined by initial rate method.

#### 4.2.6 Catecholase activity

Catecholase activity of all synthesized complexes has been evaluated. The kinetic studies involved variation in three different parameters such as substrate concentration,

catalyst concentration and temperature. The concentration and temperature employed for this activity are mentioned below in a tabular form (**Table 4.2.6.1**).

**Table 4.2.6.1** Concentration of substrate and catalyst with different parameters employed in this study

Parameters	Concentration(mM)/Temp (°C)					
<b>C9</b>						
<b>3,5-DTBC</b>	[Cat=0.06mM and Temp= 30°C]					
	Substrate	8	12	16	20	24
	[Sub=24mM and Temp= 30°C]					
	Catalyst	0.1	0.2	0.3	0.4	0.5
	[Sub=24mM and Cat=0.06mM]					
Temp	30	35	40	45	50	
<b>4-MC</b>	[Cat=0.03mM and Temp= 30°C]					
	Substrate	8.33	16.67	25		
	[Sub=8mM and Temp= 30°C]					
	Catalyst	0.2	0.3	0.4		
	[Sub=8mM and Cat=0.03mM]					
Temp	40	50	60			
<b>Dopamine</b>	[Cat=0.02mM and Temp= 30°C]					
	Substrate	30	35	40	45	50
	[Sub=24mM and Temp= 30°C]					
	Catalyst	0.05	0.1	0.15	0.2	0.25
	[Sub=24mM and Cat= 0.02mM]					
Temp	30	35	40	45	50	

**Table 4.2.6.1** (Contd...) Concentration of substrate and catalyst with different parameters employed in this study

Parameters	Concentration(mM)/Temp (°C)						
<b>C10</b>							
<b>3,5-DTBC</b>	[Cat=0.08mM and Temp= 30°C]						
	Substrate	1	2	4	6	8	10
	[Sub=4mM and Temp= 30°C]						
	Catalyst	0.06	0.08	0.1	0.12	0.14	
	[Sub=4mM and Cat=0.08mM]						
Temp	30	35	40	45	50		
<b>4-MC</b>	[Cat=0.008mM and Temp= 30°C]						
	Substrate	8	16.67	25	32	42	
	[Sub=8mM and Temp= 30°C]						
	Catalyst	0.008	0.017	0.025	0.03	0.04	
	[Sub=8mM and Cat=0.008mM]						
Temp	30	40	50				

The reaction rates, order and activation energy of reactions were calculated as explained in **section 2.2.6** in chapter 2. The initial rate method has been used for calculating the rates of the reaction.

#### ***4.2.5 Physical Measurements***

##### *4.2.5.1 Infrared studies*

Infrared Spectra ( $4000 - 400 \text{ cm}^{-1}$ ) were recorded in the form of KBr pellets at  $27^\circ\text{C}$  using Perkin Elmer RX1 FTIR spectrometer and Bruker Alpha Transmission FT-IR spectrometer. The solid sample was ground with anhydrous KBr and casted into a pellet using 10mm die and hydraulic press.

##### *4.2.5.2 NMR studies*

The  $^1\text{H}$  NMR spectra of all synthesized ligand were recorded in  $\text{DMSO-}d_6$  solutions using Bruker Avance (400 MHz) NMR spectrometer.

##### *4.2.5.3 Mass studies*

ESI-Mass of all complexes and ligands were recorded using Applied Biosystem API 2000 Mass spectrometer, XEVO G2-XS QTOF mass spectrometer and Thermo Scientific Xcalibur GC-MS spectrometer.

##### *4.2.5.4 Electronic studies*

Electronic spectra (200–900 nm) were recorded in methanolic and aqueous solutions using PerkinElmer UV-Vis spectrophotometer Model Lamda 35.

##### *4.2.5.5 Photoluminescence studies*

The emission spectra of all synthesized ligands and complexes were recorded on FP-6300 spectrofluorophotometer.

##### *4.2.5.6 Elemental Analysis*

Elemental analysis of the complexes was done using EuroVector EA 300 from SAIF CDRI Lucknow.

##### *4.2.5.7 ESR studies*

ESR of all complexes were recorded using ESR JEOL using X- band frequency with 9.2 GHz and Bruker Biospin GmbH EPR instrument with a center field of 3200G using a microwave frequency in the range of 9.45 GHz

#### 4.2.5.8 Magnetic studies

Variable temperature magnetic susceptibility measurements have been carried out in the temperature range of 90-295 K using an indigenous Faraday set up with a Mettler UMX5 ultramicrobalance at 0.8 Tesla. Diamagnetic corrections have been incorporated using Pascal constants.

#### 4.2.5.9 Single Crystal X-ray Diffraction

Single crystal diffraction data for complex C9 was collected on Bruker APEX-II CCD diffractometer (CIF IISER Bhopal). Olex2<sup>12</sup> was used for structure solving and refinement. The structure was solved by Direct Methods with SHELXS<sup>13,14</sup> structure solution program and refined by full matrix least squares method based on F2 with all observed reflections with the SHELXL<sup>13,14</sup> refinement package. Graphics were generated using MERCURY (version 4.3.1). All non-hydrogen atoms were refined with anisotropic thermal parameters. The hydrogen atoms attached to carbon were constrained to 'ride' on the atom attached to it. In all the cases, non-hydrogen atoms were treated anisotropically. Whenever possible, the hydrogen atoms were refined by locating on a difference Fourier map. In other cases, hydrogen atoms were geometrically fixed.

#### 4.2.5.10 Molecular Modelling

The geometry of the complexes was optimized using GAUSSIAN 16 software program<sup>15</sup>. Molecular geometries of the ground state of the complexes were optimized by using B3LYP method<sup>16</sup> with 6-31G and LANL2DZ basis set<sup>17,18</sup>. Molecular frontier orbitals HOMO (highest occupied molecular orbital) and LUMO (lowest unoccupied molecular orbital) were identified and visualized in Gauss View 6<sup>19</sup>.

## 4.3 RESULTS AND DISCUSSION

### 4.3.1 Characterization of ligands

#### 4.3.1.1 IR spectra

The IR spectra of ligands (**L<sup>9</sup>**, **L<sup>10</sup>** and **L<sup>12</sup>**) consist of all important bands corresponding to the stretching and bending vibrations corresponding to the aliphatic and aromatic C-H, C-C, C-O of phenol observed at their respective values as expected for the ligands. The IR spectra of synthesized ligands (**L<sup>9</sup>**, **L<sup>10</sup>** and **L<sup>12</sup>**) consist of all important bands as expected for the ligands (**Table 4.3.2.1.1**). The  $\nu_{C=N}$  stretching frequency of ligand

(**L**<sub>9</sub>, **L**<sub>10</sub> and **L**<sub>12</sub>) appears in the range 1650-1640cm<sup>-1</sup>. A band appears at ~1720.45cm<sup>-1</sup> corresponding to -C=O of cyclic ester in ligand **L**<sup>12</sup> (See SI †: **Fig. S4.1-S4.3**)

*Table 4.3.2.1.1 IR frequencies of **L**<sup>9</sup>, **L**<sup>10</sup> and **L**<sup>12</sup>*

Ligands	$\nu_{\text{C=N}}$	$\nu_{\text{C=O}}$	$\nu_{\text{O-H}}$
		(cyclic ester)	
<b>L</b> <sup>9</sup>	1643.98	-	3381.76
<b>L</b> <sup>10</sup>	1647.63	-	3243.06
<b>L</b> <sup>12</sup>	1650.78	1720.45	3430.84

#### 4.3.1.2 NMR Spectra

Ligand **L**<sup>9</sup>: <sup>1</sup>H NMR ( $\delta$  ppm in DMSO-*d*<sub>6</sub>): 2.703 (s, 6H, -CH<sub>3</sub>), 3.519 (d, 2H, -CH<sub>2</sub>-CH(OH)-CH<sub>2</sub>-), 3.751 (d, 2H, -CH<sub>2</sub>-CH(OH)-CH<sub>2</sub>-), 3.840 (m, 1H, -CH<sub>2</sub>-CH(OH)-CH<sub>2</sub>-), 5.9 (s, 1H, -CH<sub>2</sub>-CH(OH)-CH<sub>2</sub>-), 6.749 (d, 2H, naphthalene ring), 7.361 (t, 2H, naphthalene ring), 7.488 (t, 2H, naphthalene ring), 7.516 (d, 2H, naphthalene ring), 7.615 (d, 2H, naphthalene ring), 8.331-8.350 (d, 2H, naphthalene ring), 16.134 (s, 2H, Ar-OH) (see SI †: **Fig. S4.4**).

Ligand **L**<sup>10</sup>: <sup>1</sup>H NMR ( $\delta$  ppm in DMSO-*d*<sub>6</sub>): 2.512-2.592 (s, 3H, -CH<sub>3</sub>), 2.507-2.487 (s, 6H, -CH<sub>3</sub>), 7.811-7.164 (m, 14H, aromatic H) (see SI †: **Fig. S4.5**).

Ligand **L**<sup>12</sup>: <sup>1</sup>H NMR ( $\delta$  ppm in DMSO-*d*<sub>6</sub>): 2.342 (s, 3H, -CH<sub>3</sub>), (s, 6H, -COCH<sub>3</sub>), 3.708 (d, 2H, -CH<sub>2</sub>-CH(OH)-CH<sub>2</sub>-), 3.924-3.892 (d, 2H, -CH<sub>2</sub>-CH(OH)-CH<sub>2</sub>-), 5.741-5.729 (m, 1H, -CH<sub>2</sub>-CH(OH)-CH<sub>2</sub>-), 6.020 (s, 1H, -CH<sub>2</sub>-CH(OH)-CH<sub>2</sub>-), 6.553-6.530 (s, 1H, H-C-(CO)-O (cyclic ester)), 7.605-7.581 (s, 2H, Ar-H), 8.894-8.871 (d, 2H, H-C=N), 14.472 (s, 2H, Ar-OH) (see SI †: **Fig. S4.6**).

#### 4.3.1.3 Electronic spectra

The electronic absorption spectra of ligands (**L**<sup>9</sup>, **L**<sup>10</sup> and **L**<sup>12</sup>) have been recorded (**Figure 4.3.1.3.1**). The  $\pi$ - $\pi^*$  transition and n- $\pi^*$  transitions are tabulated in **Table 4.3.2.3.1**.

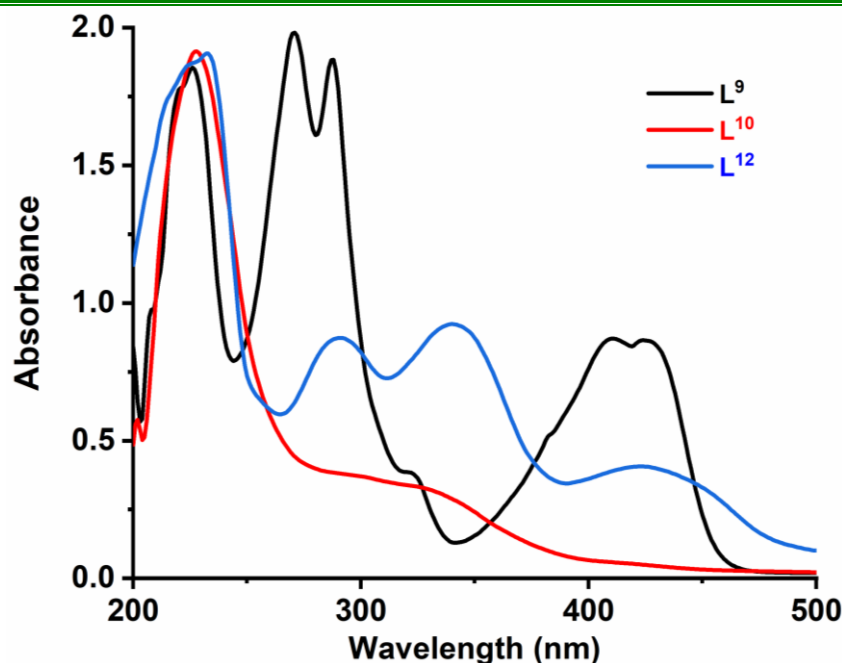


Figure 4.3.1.3.1 UV-Vis spectra of  $L^9$ ,  $L^{10}$  and  $L^{12}$  ligands

#### 4.3.1.4 Photoluminescence spectra

The emission band was observed at 495 nm when a solution of ligand  $L^9$  in DMSO was excited at  $\lambda_{\max} = 410$  nm (Figure 4.3.2.5.1(a)). The emission band was observed at 456 nm when a solution of ligand  $L^{10}$  in MeOH was excited at  $\lambda_{\max} = 410$  nm (Figure 4.3.2.5.1(b)). The emission band was observed at 497 nm when the solution of ligand  $L^{12}$  in DMSO was excited at  $\lambda_{\max} = 425$  nm. (Figure 4.3.2.5.1(c)). Thus, all three ligands are fluorescent when excited at a particular wavelength.

#### 4.3.1.5. Mass Spectra

In the mass spectrum of ligand  $L^9$  and  $L^{10}$ , a peak is observed at  $m/z = 427.2018$  corresponding to  $[M+H]^+$  where  $M =$  molecular weight of  $L^9$  and  $L^{10} = 426$ . (See SI† Fig. S4.7-S4.8) In the mass spectrum of ligand  $L^{12}$ , a peak is observed at  $m/z = 463.1495$  corresponding to  $[M+H]^+$  where  $M =$  molecular weight of  $L^{12} = 462$ . (See SI† Fig. S4.9)

### 4.3.2 Characterization of complexes

#### 4.3.2.1 Elemental analysis

All synthesized complexes were characterized by elemental analysis and was tabulated in table 4.3.2.1.1 (Values in parenthesis are calculated values)

Table 4.3.2.1.1 Elemental analysis of complexes (C9, C10 and C12)

Complex	Empirical formula (Mol. Wt.)	%C	%H	%N
<b>C9</b>	Cu <sub>2</sub> C <sub>29</sub> H <sub>26</sub> O <sub>5</sub> N <sub>2</sub> ·H <sub>2</sub> O (M.W.= 627)	55.669 (55.502)	4.674 (4.466)	4.937 (4.466)
<b>C10</b>	Cu <sub>2</sub> C <sub>29</sub> H <sub>26</sub> O <sub>5</sub> N <sub>2</sub> ·3H <sub>2</sub> O (M.W.=663)	52.950 (52.489)	4.717 (4.827)	4.107 (4.223)
<b>C12</b>	Cu <sub>2</sub> C <sub>27</sub> H <sub>22</sub> O <sub>9</sub> N <sub>2</sub> Cl <sub>2</sub> ·5H <sub>2</sub> O (M.W.=735)	43.760 (44.08)	4.191 (4.353)	5.324 (3.809)

\* The values in parentheses are calculated from the formula in column 2 of the table.

#### 4.3.2.2 IR spectra

In the IR spectra of all complexes,  $\nu_{C=N}$  appears at  $\sim 1610$ - $1640$   $\text{cm}^{-1}$  for complexes **C9-C12** (see SI†: Fig S4.10-4.12). The  $\nu_{C=N}$  stretching in all complexes has shifted to a lower frequency as compared to that in the free ligand. This clearly indicates the participation of imine N in the coordination with copper(II) ion (Table 4.3.2.2.1). A band appears at  $\sim 1720.45$   $\text{cm}^{-1}$  corresponding to the stretching of  $-C=O$  of cyclic ester group in free ligand **L<sup>12</sup>** while that in complex **C12** appears at  $1719.24$   $\text{cm}^{-1}$ . The peak at  $3400$ - $3500$   $\text{cm}^{-1}$  corresponds to the  $\nu_{O-H}$  of water molecules in complexes (**C9**, **C10** and **C12**).

Table 4.3.2.2.1 IR frequencies of complexes (C9, C10 and C12)

Complex	$\nu_{C=N}$ ( $\text{cm}^{-1}$ )	$\nu_{C=O}$ ( $\text{cm}^{-1}$ )	$\nu_{O-H}$ of water ( $\text{cm}^{-1}$ )
<b>C9</b>	1617.11	-	3438.11
<b>C10</b>	1615.67	-	3421.53
<b>C12</b>	1639.24	1719.24	3438.74

#### 4.3.2.3 Mass spectra

In the mass spectrum of complex **C9**, the peak was observed at  $m/z = 550$  due to  $[\text{Cu}_2(\text{L}_9)]^+$  (Mol wt. = 549). In the mass spectrum of complex **C10**, a peak was observed at  $m/z = 666.1$  due to  $[\text{Cu}_2(\text{L}_{10})(\text{OAc})] \cdot 3\text{H}_2\text{O}$  (Mol. Wt.= 663). In the mass spectrum of complex **C12**, a peak was observed at  $m/z = 523.0645$  due to  $[(\text{CuL}_{12}-3\text{H})]^+$  (Mol wt. = 522). The peak was observed at  $m/z = 665.004$  and  $667.0004$  due to  $[[\text{Cu}_2(\text{L})(\text{OAc})] \cdot \text{H}_2\text{O}]^+$  (Mol wt= 662) (see SI†: Fig S4.13-4.15).

## 4.3.2.4 Electronic spectra

The electronic absorption spectra of all complexes have a charge transfer band appearing at  $\lambda_{\text{max}} = 340 - 400 \text{ nm}$  which may be assigned to MLCT. All complexes have a broad ligand field band between 600-650nm in the visible region corresponding to copper(II) in a distorted ligand environment.

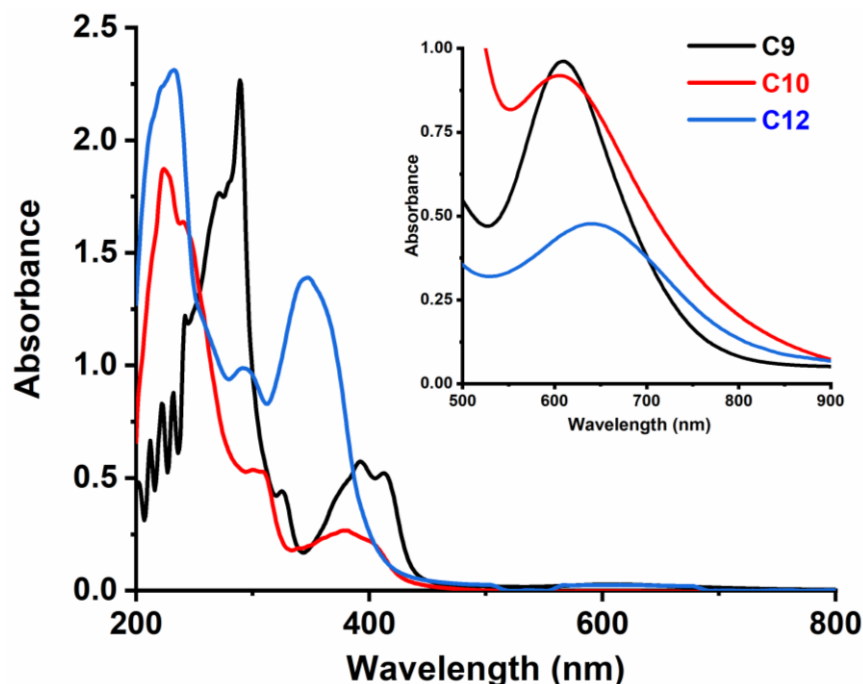


Figure 4.3.2.4.1 UV-Vis spectra of complexes (C9, C10 and C12)

The intense higher energy bands corresponding to the intra-ligand  $n-\pi^*$  and  $\pi-\pi^*$  transitions for all complexes appear between 200-350nm (**Figure 4.3.2.4.1**).

It is known that for  $d^9$  system (in octahedral geometry),  ${}^2T_{2g} \leftarrow {}^2E_g$  is expected to take place between 600 and 800 nm. On distortion to distorted octahedral or square pyramidal or trigonal bipyramidal or square planar structure, this band undergoes a significant shift and broadening due to splitting of the spectral states and multiple transitions merging to form a broad band.<sup>20</sup> In the complexes reported here, the broad band between 600-650nm may be assigned to the combination of  ${}^2E_g \leftarrow {}^2B_{1g}$ ,  ${}^2B_{2g} \leftarrow {}^2B_{1g}$ ,  ${}^2E_g$  and  ${}^2A_{1g} \leftarrow {}^2B_{1g}$  transitions, a characteristic of a  $d^9$  metal ion in distorted square-planar geometry. The observed wavelengths with  $\epsilon_{\text{max}}$  values have been tabulated below (**Table 4.3.2.4.1**).

**Table 4.3.2.4.1** Electronic spectra of ligands ( $L^9$ ,  $L^{10}$ , and  $L^{12}$ ) and complexes, (**C9**, **C10** and **C12**)

Complexes	$\lambda_{\max}/\text{nm}$ ( $\epsilon_{\max}/\text{dm}^3\text{mol}^{-1}\text{cm}^{-1}$ )		
	Intra-ligand transitions	Charge transfer	d-d transitions
<b>L<sup>9</sup></b>	224 (66428), 271(70714), 289(67142), 409(31071), 426(30892)	-	-
<b>C9</b>	270(63000), 290(181071)	391(20357), 414 (18642)	610 (960)
<b>L<sup>10</sup></b>	228(114702), 307(21411), 411(3470)	-	-
<b>C9</b>	224(252702), 305(71621)	380(37162)	605(920)
<b>L<sup>12</sup></b>	232(48000), 290(21900), 340(23150), 423(10200)	-	-
<b>C12</b>	232(57750), 293(24670),	346(34800)	639(481)

#### 4.3.2.5 Photoluminescence spectra

The emission band was observed at 495nm when a solution of ligand **L<sup>9</sup>** in DMSO was excited at  $\lambda_{\max} = 410$  nm but emission band was observed at 505 nm when a solution of the complex **C9** in DMSO was excited at  $\lambda_{\max} = 415$ nm. Also a decrease in fluorescence intensity was observed (**Figure 4.3.2.5.1(a)**). An emission band was observed at 456nm when a solution of ligand **L<sup>10</sup>** in methanol was excited at  $\lambda_{\max} = 410$  nm but the complex **C10** in methanol is not fluorescent even when excited at  $\lambda_{\max} = 380$ nm (**Figure 4.3.2.5.1(b)**). The emission band was observed at 497 nm when the solution of ligand **L<sup>12</sup>** in DMSO was excited at  $\lambda_{\max} = 425$  nm. However, the complex **C12** does not show any fluorescence even when excited at  $\lambda_{\max} = 346$ nm in DMSO (**Figure 4.3.2.5.1(c)**). Thus, all three ligands are fluorescent but only the complex **C9** was found to be fluorescent with a small shift and decrease in the intensity of the emission band. The Fluorescence of ligands **L<sup>10</sup>** and **L<sup>12</sup>** is completely quenched in presence of copper(II) ion in their complexes. This implies a possible application of these ligands as fluorescence sensors for copper(II) ions.

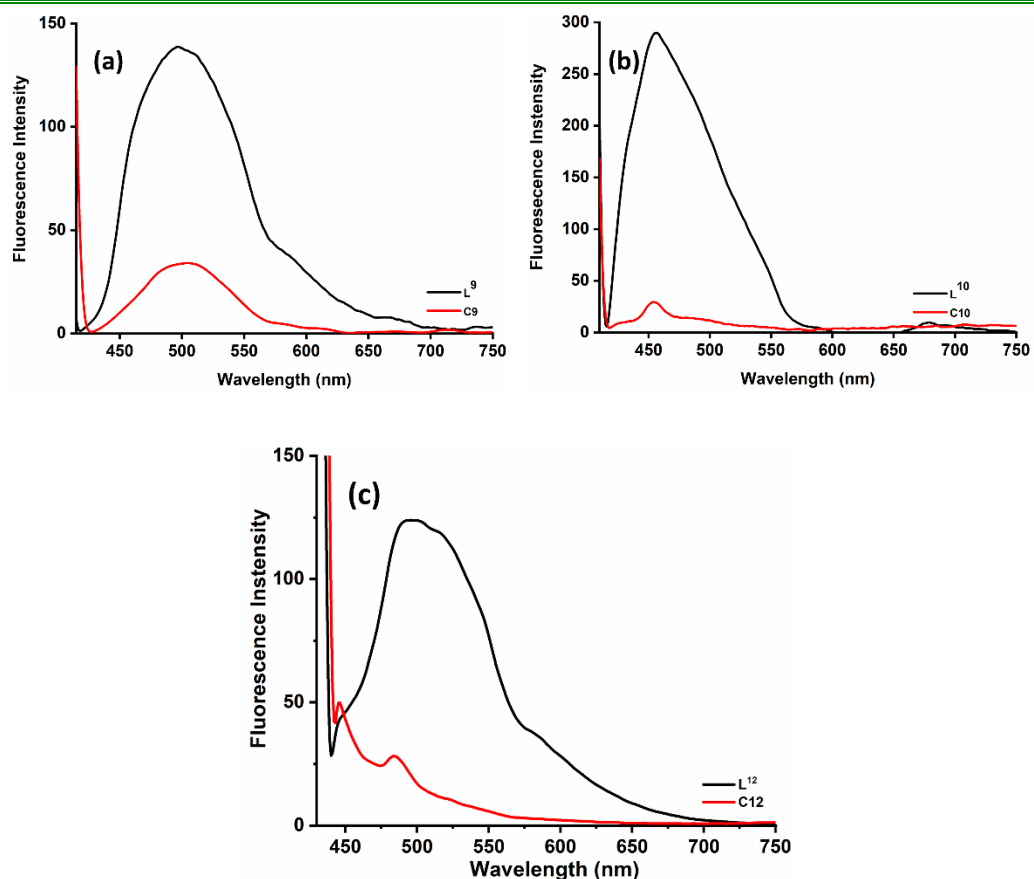


*Figure 4.3.2.5.1 Emission spectra of (a) L<sup>9</sup> & C<sub>9</sub>, (b) L<sup>10</sup> and C<sub>10</sub> and (b) L<sup>12</sup> and C<sub>12</sub>*

#### 4.3.2.6 Crystal structure of complex C<sub>9</sub>

Dark green rectangular plates like crystals were obtained by very slow evaporation of a solution of complex C<sub>9</sub> in dichloromethane as solvent. This required about 20-25 days. The crystal structure of the complex C<sub>9</sub> was determined and is shown in **figure 4.3.2.6.1**. The crystal data and structure refinement parameters of complex C<sub>9</sub> are given in **table 4.3.2.6.1**. Bond distances and bond angles relevant to metal coordination sphere of complex C<sub>9</sub> are given in **Table 4.3.2.6.2**.

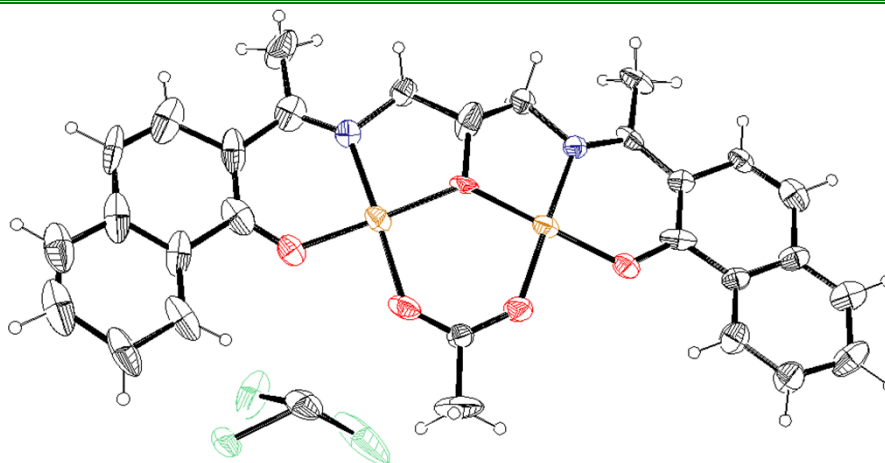


Figure 4.3.2.6.1 ORTEP representation (30% ellipsoid probability) of complex C9

Table 4.3.2.6.1 Crystal data and structure refinement for complex C9

Identification code	C9
Empirical formula	Cu <sub>2</sub> C <sub>29</sub> H <sub>26</sub> N <sub>2</sub> O <sub>5</sub> Cl <sub>2</sub>
Formula weight	680.50
Temperature/K	140.00
Crystal system	monoclinic
Space group	P2 <sub>1</sub> /c
a/Å	11.2534(19)
b/Å	17.310(3)
c/Å	15.459(3)
α/°	90
β/°	110.390(6)
γ/°	90
Volume/Å <sup>3</sup>	2822.6(8)
Z	56
ρ <sub>calc</sub> /cm <sup>3</sup>	22.419
μ/mm <sup>-1</sup>	24.338
F(000)	19376.0
Crystal size/mm <sup>3</sup>	? × ? × ?
Radiation	MoKα (λ = 0.71073)
2θ range for data collection/°	3.666 to 50.252
Index ranges	-13 ≤ h ≤ 13, -20 ≤ k ≤ 20, -18 ≤ l ≤ 18
Reflections collected	42564
Independent reflections	5034 [R <sub>int</sub> = 0.2812, R <sub>sigma</sub> = 0.1157]
Data/restraints/parameters	5034/0/382
Goodness-of-fit on F <sup>2</sup>	2.171
Final R indexes [I ≥ 2σ(I)]	R <sub>1</sub> = 0.1426, wR <sub>2</sub> = 0.3833
Final R indexes [all data]	R <sub>1</sub> = 0.2008, wR <sub>2</sub> = 0.4169
Largest diff. peak/hole / e Å <sup>-3</sup>	2.03/-1.22

Accordingly, the stereochemistry around each copper(II) centre can be best described as distorted square planar geometry in complex **C9**. The doubly bridged  $\mu$ -alkoxo and  $\mu$ -acetate oxygen atoms occupy the equatorial positions, and the coordination geometry around the copper(II) ion through imine nitrogen atom and phenoxo oxygen donors from the acetonaphthones in complex **C9**. The Cu-O (alkoxo) distances Cu1-O1 and Cu2-O1 are 1.9010(10) and 1.889(11) Å, respectively, in complex **C9**, which shows that the bridging by phenolic oxygens is almost symmetrical. The basal Cu-O distances are comparable in lengths, showing Cu1-O4=1.938(12) and Cu2-O5=1.960(10) for the acetate oxygen (Table 4.3.2.6.2.). The Cu1-O1-Cu2 bond angle is 131.2(5) leading to a Cu1...Cu2 non-bonding distance between the two metal ions of 3.461 Å in **C9**.

Both copper nuclei are coordinated by one nitrogen containing group and other oxygen containing group. Cu1 and Cu2 are coordinated by one sp<sup>2</sup> nitrogen, imine nitrogen (N1 for Cu1 and N2 for Cu2), one alkoxo oxygen and an oxygen of the bridging acetate in complex **C9**. It should be noted that all the Cu–N distances fall in the range 1.930–1.950 Å. The N1-Cu1-O1, N1-Cu1-O2, O2-Cu1-O4 and O4-Cu1-O1 angles are 86.6(5), 91.3(5), 86.2(5) and 95.9(5), respectively. The N2-Cu2-O1, N2-Cu2-O3, O3-Cu2-O5 and O5-Cu2-O1 angles are 85.6(4), 92.9(5), 85.3(4) and 96.3(4), respectively, indicating near square planar / slightly distorted square planar geometry around the copper ions in complex **C9**.

*Table 4.3.2.6.2 Bond Lengths and Angles related to metal coordination in complex C9*

Atom -Atom	Bond length	Atom-Atom-Atom	Bond Angles
Cu1-O1	1.910(10)	N1-Cu1-O1	86.6(5)
Cu1-N1	1.938(13)	N1-Cu1-O2	91.3(5)
Cu1-O2	1.891(11)	O2-Cu1-O4	86.2(5)
Cu1-O4	1.938(12)	O4-Cu1-O1	95.9(5)
Cu2-O1	1.889(11)	N2-Cu2-O1	85.6(4)
Cu2-N2	1.889(11)	N2-Cu2-O3	92.9(5)
Cu2-O3	1.864(11)	O3-Cu2-O5	85.3(4)
.Cu2-O5	1.960(10)	O5-Cu2-O1	96.3(4)
Cu1-Cu2	3.461	Cu1-O1-Cu2	131.2(5)

## 4.3.2.7 ESR spectra

The ESR spectra of complex **C9** and **C10** were recorded both in powdered and solution state at liquid nitrogen temperature (LNT) and while that for **C12** were recorded in powdered (RT) and solution state (LNT) (**Table 4.3.2.7.1**).

**Table 4.3.2.7.1**  $g_{\parallel}$ ,  $g_{\perp}$  and  $A_{\parallel}$  or  $A_{\perp}$  values of all complexes (**C9**, **C10** and **C12**)

Complex	$g_{\parallel}$	$g_{\perp}$	$A_{\parallel} \times 10^{-4} \text{ cm}^{-1}$
<b>C9</b>	EPR silent		
<b>C10</b>	2.28	2.01	160
<b>C12</b>	2.18 (RT)	2.08(RT)	-

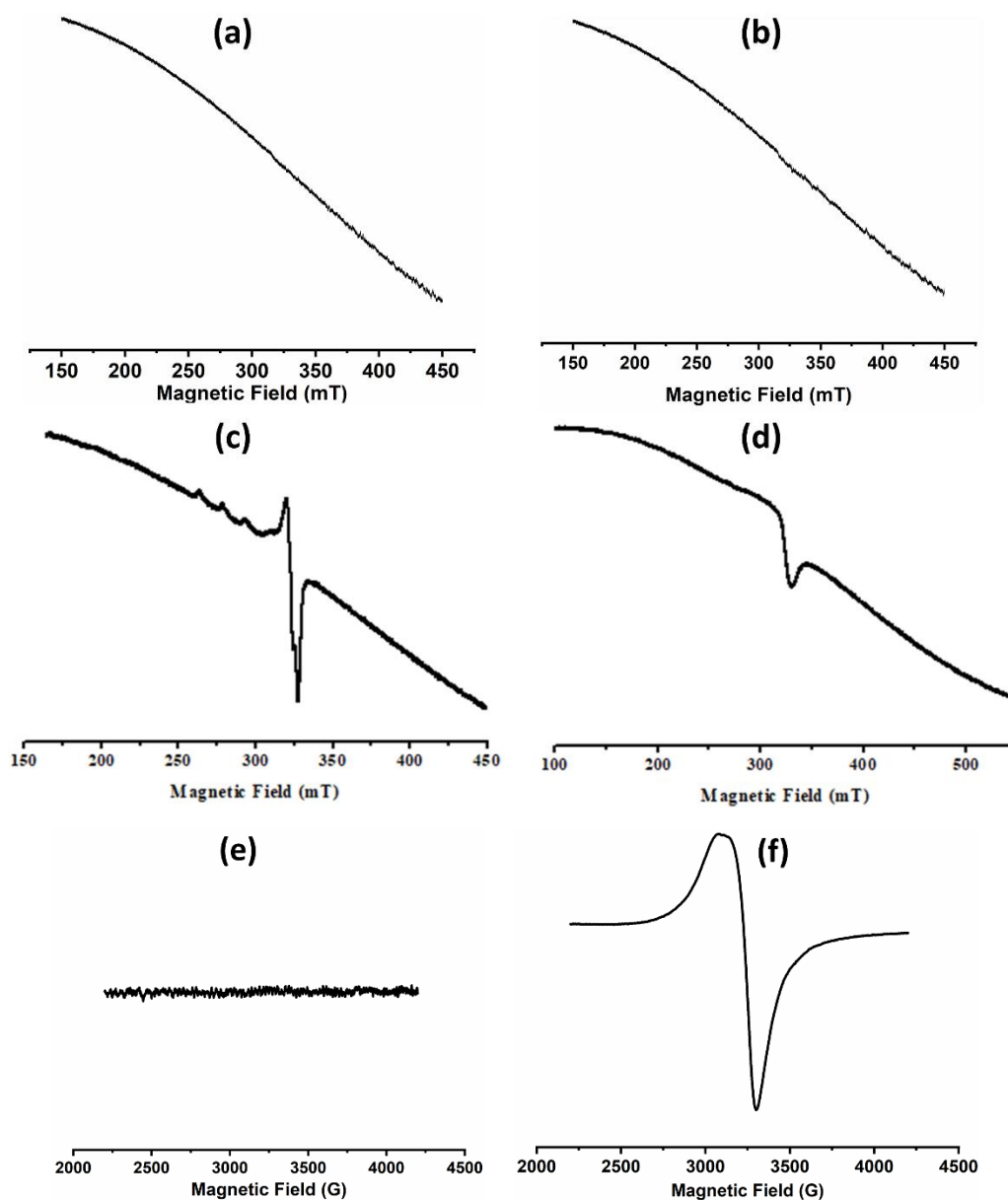


**Figure 4.3.2.7.1** ESR spectra of complexes at LNT (a) **C9**(DMSO) (b) **C9** (powder) (c) **C10** (Methanol) (d) **C10** (powder) and (e) **C12** (DMSO) (f) **C12** (powder) (RT)

The ESR spectrum of **C9** in the powdered form and in the form of frozen DMSO solution at 77K, is EPR silent indicating the presence of antiferromagnetic interaction between the copper(II) ions. Similarly, the ESR spectrum of **C12** recorded in the form of frozen DMSO solution at 77K, is EPR silent while the powdered sample has axial pattern when recorded at RT. This indicates a moderate antiferromagnetic in the complex.

The ESR spectrum of **C10** recorded in the powder form and in frozen solution at LNT is consistent with axial pattern. A well resolved hyperfine structure in the  $g_{\parallel}$  region is observed with four discernible lines in complex **C10** (Figure 4.3.2.7.1). The  $A_{\parallel}$  values are typical of the copper(II) ion present in moderately hard, NO<sub>3</sub> or N<sub>2</sub>O<sub>2</sub> coordination environment.

#### 4.3.2.8 Magnetic studies

Variable temperature magnetic study of **C9** and **C10** complexes were performed in the temperature range of 100–295 K as described in section 2.3.2.7 of chapter 2.

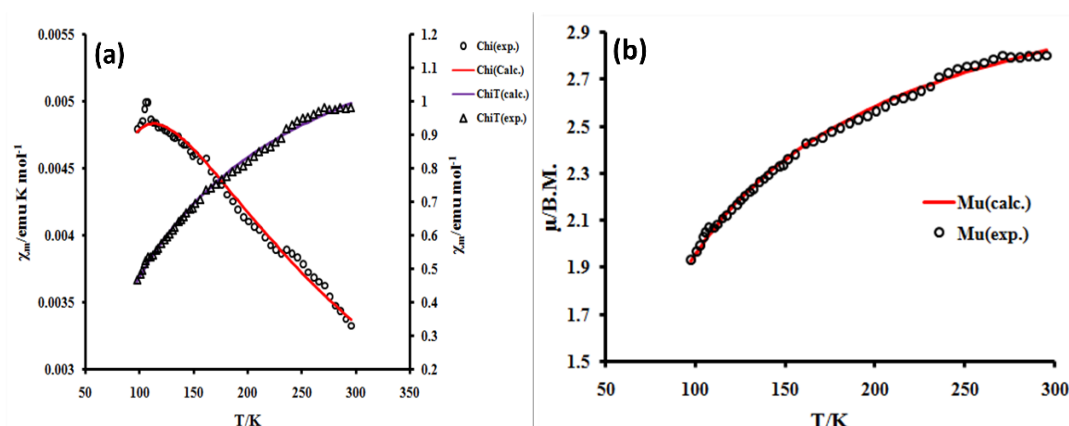


Figure 4.3.2.8.1 (a) Plot of  $\chi_m T$  and  $\chi_m$  vs  $T$  and (b)  $\mu$  vs  $T$  for complex **C9**

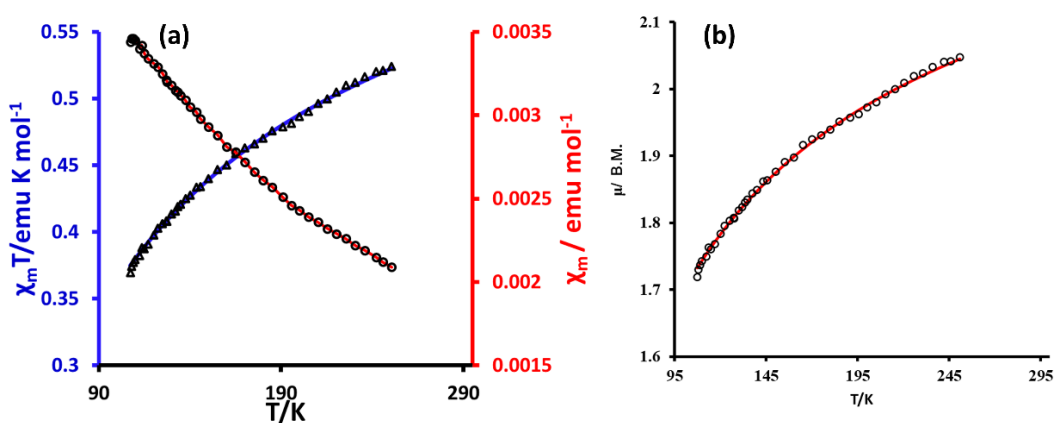


Figure 4.3.2.8.2 (a) Plot of  $\chi_m T$  and  $\chi_m$  vs  $T$  and (b)  $\mu$  vs  $T$  for complex **C10**

Plots of  $\chi_m T$  and  $\chi_m$  vs T and  $\mu$  vs T for complex **C9** and **C10**, both, clearly indicate antiferromagnetic character. ((**Figure 4.3.2.8.1** and **Figure 4.3.2.8.2**)

It is known that alkoxo- and phenoxido- bridged dicopper(II) species exhibit antiferromagnetic interaction when the M-O-M bond angle is larger than  $97.60^\circ$ . The antiferromagnetic character increases with increase in angle<sup>21</sup>. The very strong antiferromagnetic exchange coupling has also been observed in structurally closely related dicopper(II) centres bridged by phenoxide ligands<sup>22,23</sup> and those of the macrocyclic complexes<sup>24</sup>. The J value observed for the complex **C9** is  $-79.3239 \pm 1.0923$   $\text{cm}^{-1}$  and that of **C10** is  $-42.1843 \pm 0.6224$   $\text{cm}^{-1}$  with  $\chi_{\text{TIP}} = 120 \times 10^{-6}$   $\text{cm}^3 \text{mol}^{-1}$  and  $\rho = 0.001$  (0.1%). The moderately strong antiferromagnetic exchange is a result of Cu1-O-Cu2 bridge angle of  $131.2(5)^\circ$  as observed in the crystal structure for **C9** and that of complex **C10** is  $136.4(5)^\circ$  as observed in the DFT optimised structure (next section). Magneto-structural correlation in phenoxo-bridged dicopper(II) complexes reveals that the dominant pathway for super exchange through the oxygen bridge atoms involves interaction of the two copper ( $dx^2-y^2$ ) orbitals and s and p orbitals on the oxygen through predominantly  $\sigma$  overlap<sup>25</sup>. Generally, phenoxido-bridged coplanar dicopper complexes with Cu-O<sub>ph</sub>-Cu bridge angles of greater than  $99^\circ$  can have exchange coupling values as high as  $420$   $\text{cm}^{-1}$  and for the complexes with bridge angles of  $<99^\circ$ , the exchange interaction is  $<70$   $\text{cm}^{-1}$ <sup>26</sup>. Thus, the antiferromagnetic exchange interaction between the copper(II) centers is likely to be influenced by the degree of planarity of the oxygen bridges, phenoxide bridge angle and the extent of out-of-plane displacement ( $\tau$ ) of the phenyl ring from oxygen atom within Cu<sub>2</sub>O<sub>2</sub> core<sup>27,28</sup>. The intra and inter dimer chloride bridges appear to have significant influence besides phenoxides bridges in propagating the spin exchange. The J values observed for the complexes **C9** is ( $-79.32\text{cm}^{-1}$ ) and **C10** is ( $-42.18$   $\text{cm}^{-1}$ ) are consistent with their structure and observations recorded in the literature.

#### 4.3.2.9 Quantum chemical calculations

Computational studies for the electronic structure of complexes **C9**, **C10** and **C12** were calculated in order to explain their theoretical geometrical parameters in the gas phase using GAUSSIAN 16 program<sup>15,17-19</sup>. The calculated bond parameters are tabulated (see SI in **Table. S4.1**). The geometries of the complexes were optimized by B3LYP basis set (**figure 4.3.2.9.1**). Contour plots of HOMO and LUMO and their energy gap  $\Delta E_g$  is shown in **figure 4.3.2.9.2**) which plays an essential criteria for enzymatic

biological activity<sup>29</sup>. They give an idea that the chemical molecule interacts with the other species. Hence, they are called frontier molecular orbitals. LUMO and HOMO acts as electron acceptor and electron donor<sup>30</sup>. Theoretical transition energy levels between HOMO and LUMO frontier molecular orbitals were calculated by B3LYP and LANL2DZ methods in complexes **C9**, **C10** and **C12** and are tabulated in **table 4.3.2.9.1**). This  $\Delta E_g$  value reflects upon its catalytic activity<sup>31,32</sup>. The  $\Delta E_g$  value for complex **C10** is lowest which reflects the relationship with SOD mimic activity and could be considered as an active centre for SOD mimics<sup>31,32</sup>. **Figure 4.3.2.9.3** shows the graphical representations of ESP for complexes **C9**, **C10** and **C12**. The energy gap ( $\Delta E_g$ ) of the complexes were observed to have following order: **C9=C10<C12**.

*Table 4.3.2.9.1 Global reactivity descriptors of complexes in eV calculated by DFT/B3LYP/LANL2DZ basis set*

Molecular Properties	Mathematical Description	C9	C10	C12
$E_{\text{HOMO}}$	Energy of HOMO	-4.9862	-4.9372	-5.5898
$E_{\text{LUMO}}$	Energy of LUMO	-3.8063	-3.8161	-4.3331
<b>Energy gap</b>	$\Delta E_g = E_{\text{LUMO}} - E_{\text{HOMO}}$	1.1799	1.1211	1.2567
<b>Ionization potential (IP)</b>	$IP = -E_{\text{HOMO}}$	4.9862	4.9372	5.5898
<b>Electron Affinity (EA)</b>	$EA = -E_{\text{LUMO}}$	3.8063	3.8161	4.3331
<b>Electronegativity (<math>\chi</math>)</b>	$\chi = -\frac{1}{2}(E_{\text{HOMO}} + E_{\text{LUMO}})$	4.3963	4.3767	4.9615
<b>Chemical Potential (<math>\mu</math>)</b>	$\mu = \frac{1}{2}(E_{\text{HOMO}} + E_{\text{LUMO}})$	-4.3963	-4.3767	-4.9615
<b>Global Hardness (<math>\eta</math>)</b>	$\eta = -\frac{1}{2}(E_{\text{HOMO}} - E_{\text{LUMO}})$	0.5900	0.5606	0.6284
<b>Softness (S)</b>	$S = 1/2\eta$	0.8475	0.8258	0.7957
<b>Electrophilicity index (<math>\omega</math>)</b>	$\omega = \mu^2/2\eta$	16.3800	15.7860	19.5873

The energy gap ( $\Delta E_g$ ),  $E_{\text{HOMO}}$  and  $E_{\text{LUMO}}$  values are important for the prediction of global reactivity descriptors, which in details explains the internal charge transfer, stability and reactivity of the molecule<sup>32</sup>. Global reactivity descriptors such as electronegativity ( $\chi$ ), global hardness ( $\eta$ ), global electrophilicity ( $\omega$ ) and global softness ( $\sigma$ ) are calculated using the formulas based on Koopmans theorem<sup>33</sup> (equations 2.3 to 2.7 in chapter 2 **section 2.3.2.9**) (**Table 4.3.2.9.1**).

The optimized structures of all synthesized complexes (**C9**, **C10** and **C12**) are depicted in **figure 4.3.2.7.1**. Each copper(II) ions are four coordinated in all complexes **C9**, **C10** and **C12**. In all complexes, both copper ions are coordinated by alcoholic oxygen, imine nitrogen, phenoxo oxygen of acetonephthones (complex **C9** & **C10**) or of coumarin unit (for complex **C12**). Besides these, some important geometrical parameters such as bond angles, bond lengths, torsion angle related to the complexes are tabulated in supplementary information (See SI† **Table S4.1**).

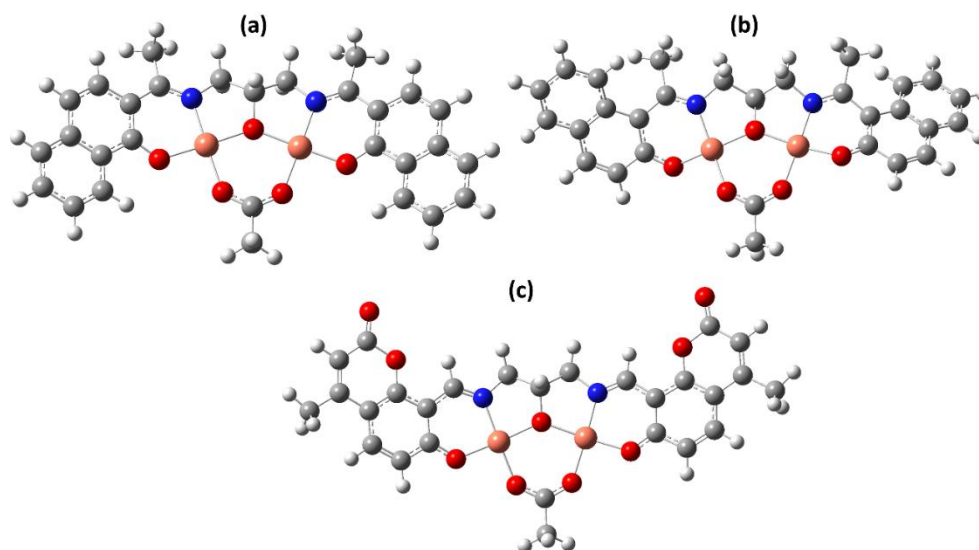


*Figure 4.3.2.9.1 DFT optimized structure of complexes (a)**C9** (b) **C10** and (c) **C12***

The calculated bond lengths of Cu-N and Cu-O of these complexes are comparable to those reported for four coordinated complexes obtained from single crystal X-ray data. In all the complexes, HOMO and LUMO along with their two upper and two lower orbitals exhibit different localization, indicating intramolecular electron charge transfer within the molecule. The energy gap ( $\Delta E_g$ ) value is directly associated with the stability and hardness and inversely related with the reactivity and softness of the molecule. A very small energy gap value shows that there is an easy charge transfer within the molecule, which may further increase the biological activity of the complex.

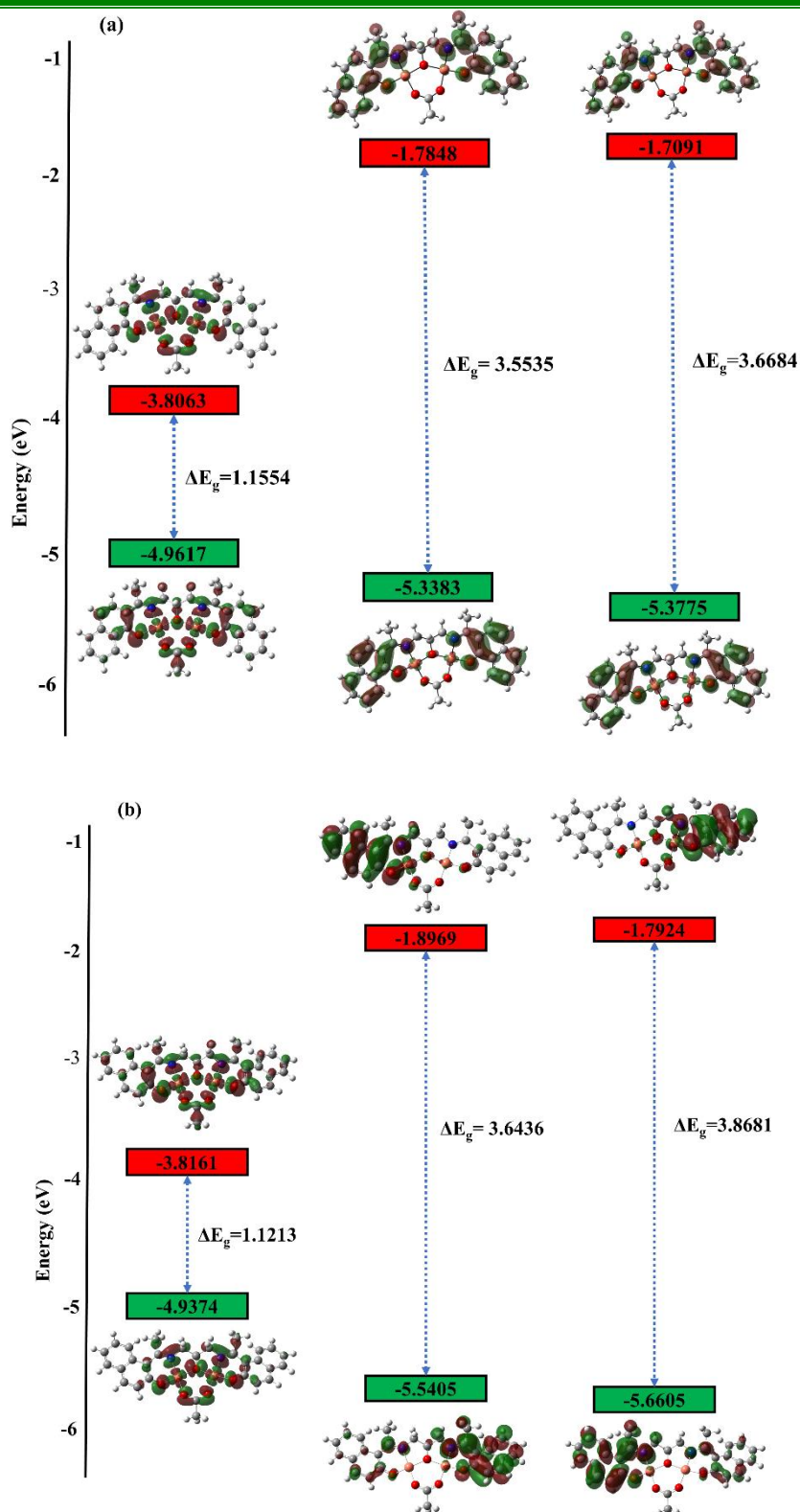


Figure 4.3.2.9.2 Frontier molecular orbitals of complexes (a) C9 (b) C10

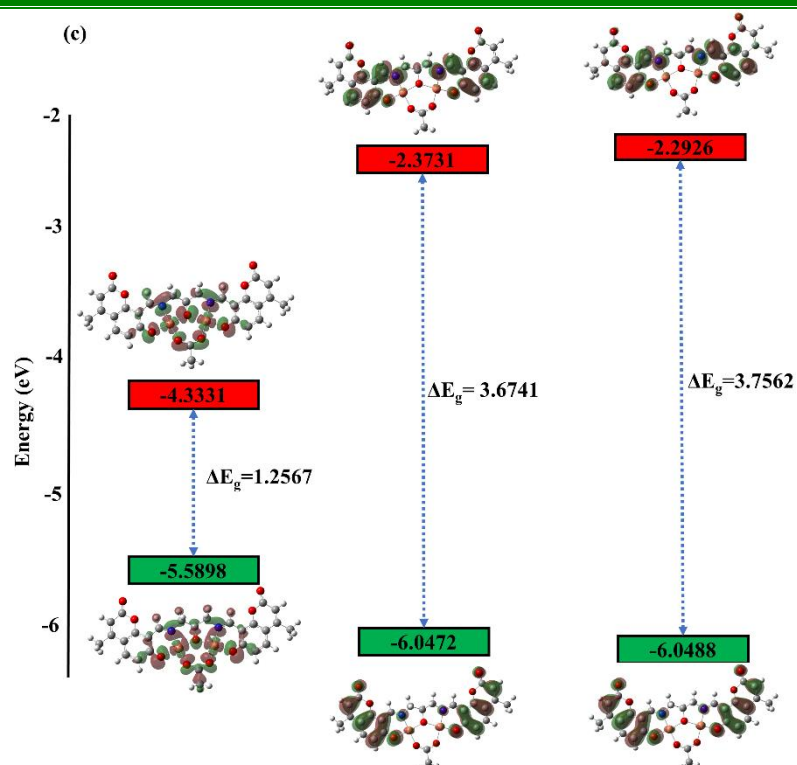


Figure 4.3.2.9.2 (Contd...) Frontier molecular orbitals of complex (c) C12

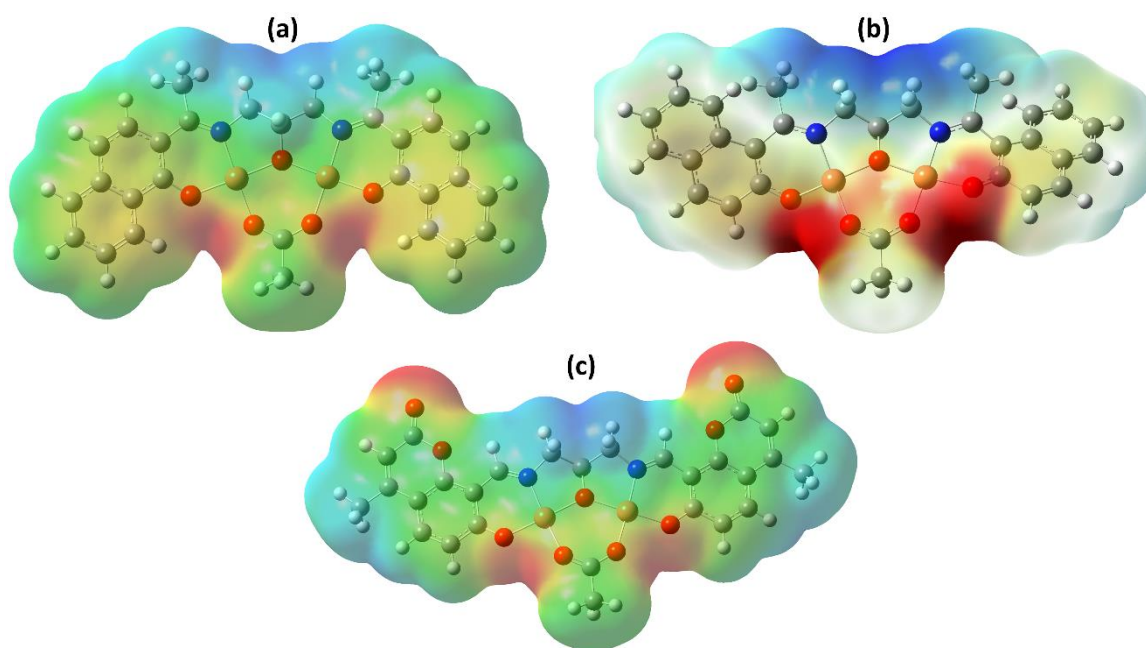
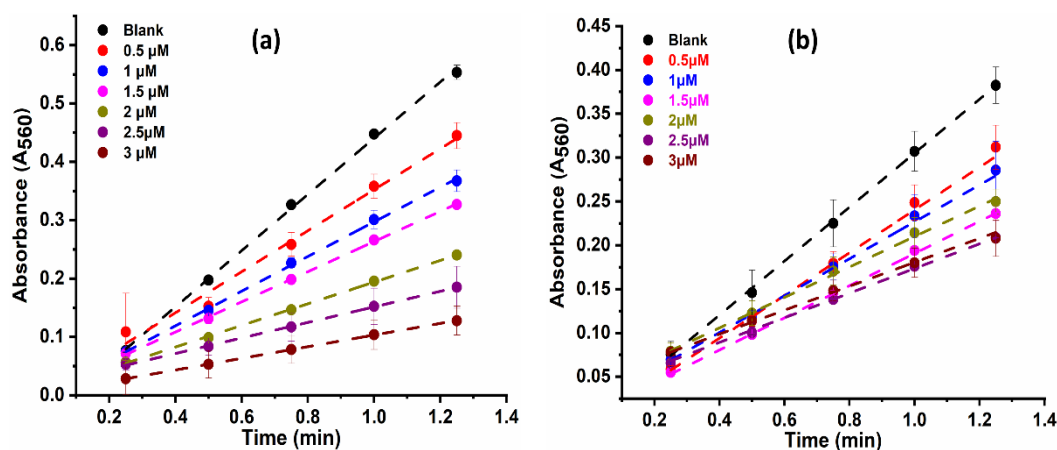


Figure 4.3.2.9.3 Electrostatic potential of complexes (a) C9 (b) C10 and (c) C12

### 4.3.3 SOD mimic activity

Generation of superoxide anion ( $O_2^{\cdot-}$ ) is responsible for the conversion of NBT to monoformazan complex and its scavenging from the system by the complexes as shown in **scheme 2.2.4.1** (chapter 2 **section 2.2.4**). The hydrogen donor NADH reduces PMS. This reduced PMS generates  $O_2^{\cdot-}$  from dissolved  $O_2$ . NBT gets reduced by  $O_2^{\cdot-}$ , which results in a linear accumulation of blue formazan with increase in the absorbance at 560nm (**Scheme 2.3.3.1** in chapter 2 **section 2.3.3**).

In the reaction medium, SOD or SOD mimic compounds scavenge  $O_2^{\cdot-}$  which results in decrease in the formation of formazan. The % inhibition of NBT reduction at various concentrations of complexes as a function of time was measured by measuring the absorbance at 560nm. **Figure 4.3.3.1** represents the plot of absorbance ( $A_{560}$ ) of blue formazan against time (t) with varying concentration of complexes. The complexes have higher values of % inhibition of the NBT reduction than those exhibited by copper salt. All ligands show very low % inhibition at 100 $\mu$ M concentration of ligand. The % inhibition of NBT reduction was found to be 0.70 %, 25.42% and 12.49%, respectively, for **L<sup>9</sup>**, **L<sup>10</sup>** and **L<sup>12</sup>** at that concentration. This confirms that none of the three ligands show appreciable SOD mimicking activity (**Figure 4.3.3.1 (d)**).



**Figure 4.3.3.1** Plot of Absorbance ( $A_{560}$ ) of blue formazan at 560nm as a function of time (min) with varying concentrations for each complexes and ligands (a) **C9** (b) **C10**

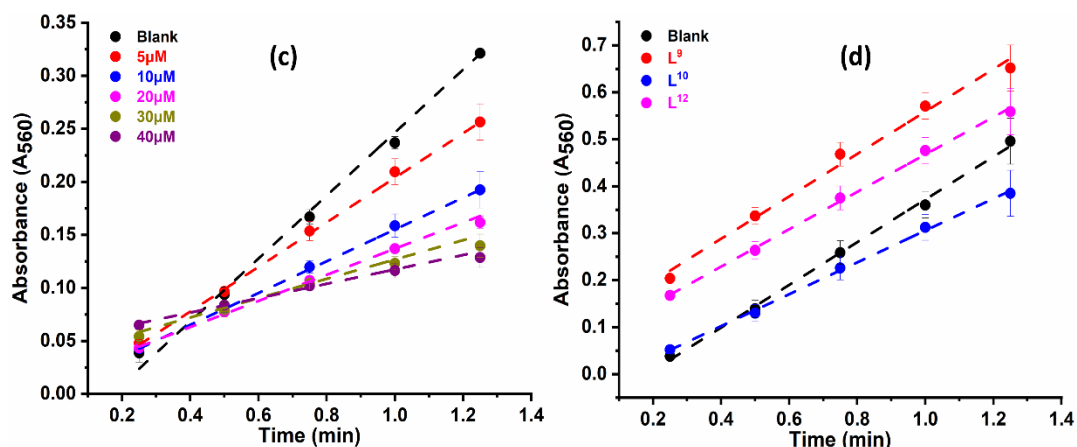


**Figure 4.3.3.1** (Contd..) Plot of Absorbance ( $A_{560}$ ) of blue formazan at 560nm as a function of time (min) with varying concentrations for each complexes and ligands (c) C12 and (d)  $L^9$ ,  $L^{10}$  and  $L^{12}$

**Figure 4.3.3.2** represents % inhibition of NBT reduction as a function of increasing concentrations of complexes which gives  $IC_{50}$  value of that particular complex. The  $IC_{50}$  values are calculated from the plots as the scavenger concentrations causing 50% inhibition of reduction of NBT.

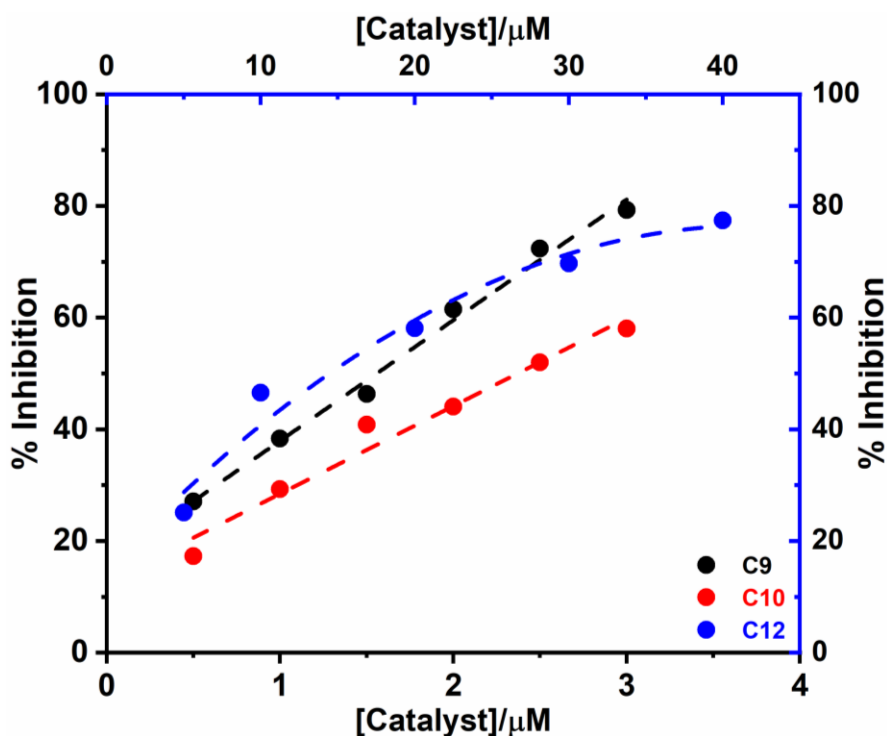


**Figure 4.3.3.2** Plot of % inhibition of NBT reduction vs. concentration of complexes

All three dicopper(II) complexes showed SOD mimic activity at the biological pH. The results show that these complexes can very efficiently scavenge superoxide radicals with IC<sub>50</sub> values ranging between 1.55-13.17 μM. These complexes have lower IC<sub>50</sub> values and hence have better SOD mimic activity than the SOD mimics reported in the literature.<sup>8,9,11,34-36</sup> The results of SOD mimic activity have been summarized below in the tabular form (**Table 4.3.3.1**).

**Table 4.3.3.1** IC<sub>50</sub> values of ligands, (*L*<sup>9</sup>, *L*<sup>10</sup> and *L*<sup>12</sup>) and complexes (*C9*, *C10* and *C12*) and native enzyme

Complexes	IC <sub>50</sub> /μM
<b>L<sup>9</sup></b>	>100
<b>C9</b>	1.5582
<b>L<sup>10</sup></b>	>100
<b>C10</b>	2.4163
<b>L<sup>12</sup></b>	>100
<b>C12</b>	13.1729
<b>Native enzyme (SOD)</b>	0.04

#### 4.3.4 Ascorbic Acid Oxidase (AAO) activity

The oxidation of AA as catalyzed by complexes under aerobic conditions in acetate buffer (pH 5.5) was monitored by measuring the absorbance of ascorbic acid band at  $\lambda_{\max} = 265\text{nm}$  using UV-Vis spectroscopy. A distinct absorption maximum at  $\lambda_{\max} = 265\text{nm}$  (marked as 'a') was observed for ascorbic acid (AA) as seen in **figure 4.3.4.1 (a)**. However, when any of these complexes was added to the solution of AA under aerobic conditions, a significant decrease in absorbance (marked as 'b') was noted which demonstrated the fact that AA was consumed in a reaction (**figure 4.3.4.1 (a)**). When same experiment was carried out under nitrogen atmosphere, there was no significant decrease in the absorbance at  $\lambda_{\max} = 265\text{nm}$  (marked as 'c') which confirms the involvement of O<sub>2</sub> in the reaction (**figure 4.3.4.1(a)**). In a control experiment, similar reaction was carried out in presence of corresponding copper salts, there was a significant decrease in the absorbance at  $\lambda_{\max} = 265\text{nm}$  (marked as 'd'). But the reaction was stoichiometric and not catalytic (**figure 4.3.4.1 (a)**). The time dependent (0-40 mins) changes in the absorption spectra upon oxidation of AA by O<sub>2</sub> in the presence of complexes was depicted in figure 4.3.4.1(b) for complex **C9** and for other complexes (see SI†: **Fig. S4.16A-B (a,e)**). The absorbance band at  $\lambda_{\max} = 265\text{nm}$  decreases with time from 0 min to 40 min and completely disappears after 40 min which confirms that

complexes quickly catalyze the oxidation of ascorbic acid to dehydroascorbic acid (DHAA). These results confirm that the complexes can activate the molecular oxygen and possess ascorbic acid oxidase mimetic activity under aerobic conditions. Hence, from these it can be concluded that the complexes have better ascorbic acid oxidase mimetic activity that can catalyze the oxidation of AA to DHAA in the presence of  $O_2$  as compared to the other complexes reported in literature<sup>37–39</sup>.

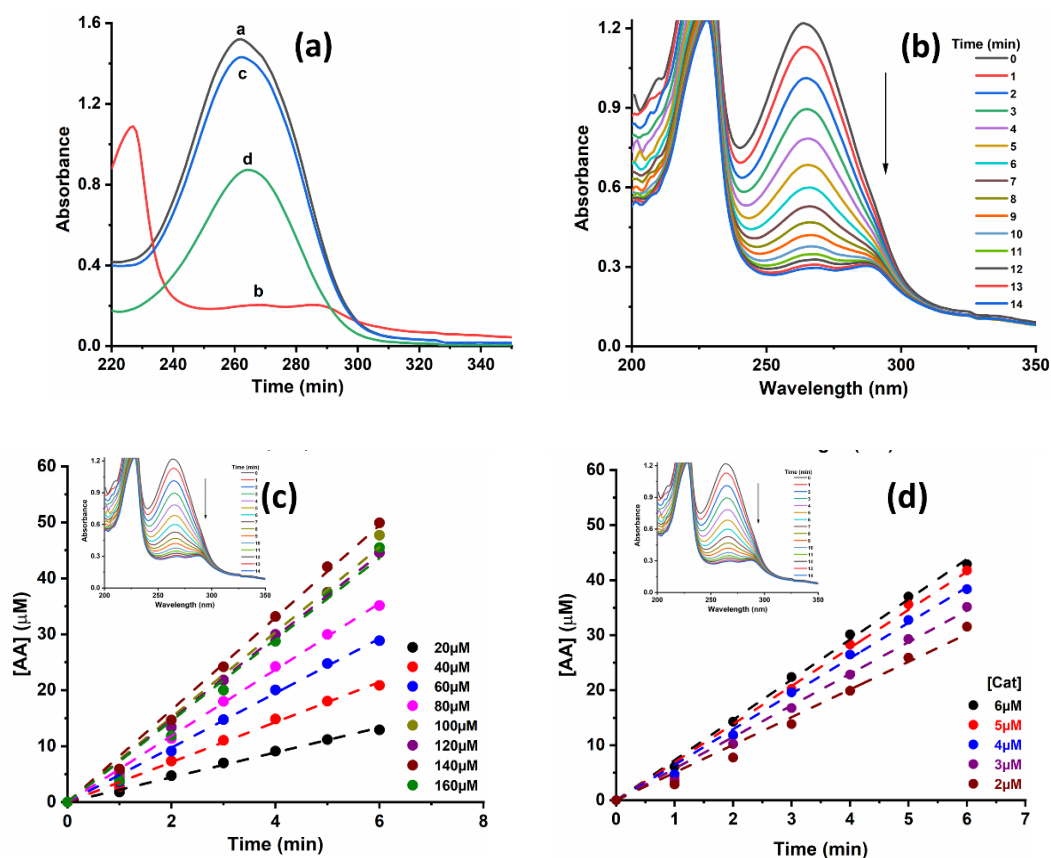


**Figure 4.3.4.1** (a) Uv-Vis spectra of a: AA, b: AA+C9 under aerobic conditions, c: AA+C9 under a  $N_2$  atm. for 20 mins and d: AA+ Cu(OAc)<sub>2</sub> for 20 mins under aerobic conditions, (b) Time dependent spectral changes from 0 to 14 mins of AA corresponding to C9 catalyzed Oxidation, (c-d) Plot of [AA] as function of time with respect to substrate concentration (c), catalyst concentration (d) (Inset: Plot of absorbance vs wavelength at different time intervals)

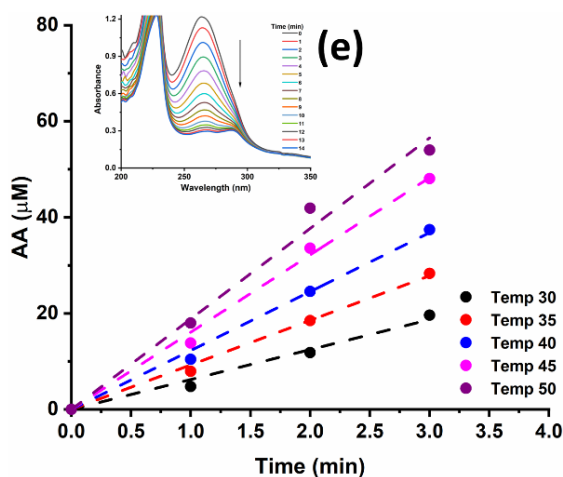


**Figure 4.3.4.1** (Contd...) (e) Plot of [AA] as function of time with respect to temperature (Inset: Plot of absorbance vs wavelength at different time intervals)

Rate of reaction for all complexes was obtained by initial rate method by plot of [AA] as function of time and using  $\epsilon = 14500 \text{ dm}^3\text{mol}^{-1}\text{cm}^{-1}$  for ascorbic acid. **Figure 4.3.4.1(c-e)** shows plot of [AA] as function of time for complex **C9** and for other complexes (see SI†: **Fig. S4.16A-B (b-d,f-h)**). To obtain the steady-state kinetic parameters, we further studied the catalytic behaviour of complexes with AA as substrate, built on enzyme kinetics theory and methods. The most commonly and widely used models and methods to study the enzymatic reaction was Michaelis-Menten model. In **figure 4.3.4.2**, the solid circles are experimental data and the solid curves are the fits to the Michaelis-Menten model for all complexes.

With various concentrations of ascorbic acid (AA), Michaelis-Menten constant ( $K_m$ ) has been calculated using the Michaelis-Menten equation 2.8 as described in section 2.3.4 of chapter 2 and by Lineweaver-Burk plot. With the help of parameters  $K_m$  and catalytic rate ( $k_{cat}$ ), the kinetics of the enzymatic reactions can be understood.

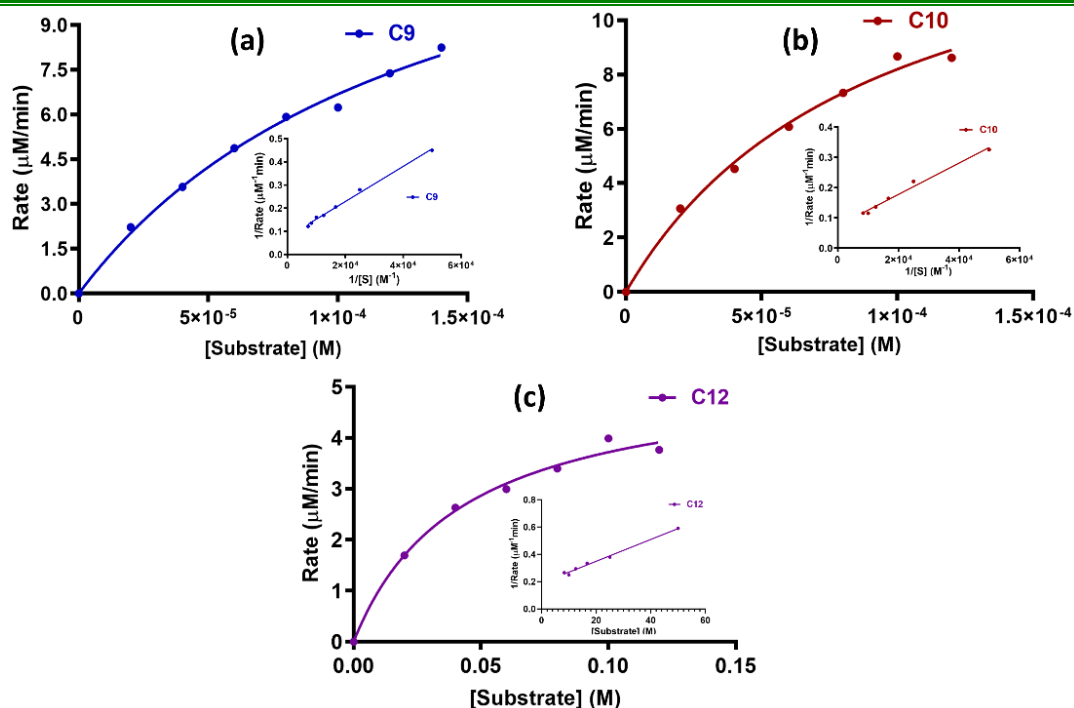


**Figure 4.3.4.2** Rate vs [substrate] plot of Michaelis-Menten model for complexes (a) C9 (b) C10 and (c) C12 (Inset: Lineweaver Burk plot of respective complexes)

The order of reaction with respect to substrate was obtained from slope of the plot of  $\log(\text{rate})$  as function of  $\log[\text{substrate}]$  (**Figure 4.3.4.3**). Similarly, the order with respect to the catalyst was obtained from the plot of  $\log(\text{rate})$  as function of  $\log[\text{catalyst}]$  (**figure 4.3.4.4**). The order of the reaction was found to be half order with respect to the substrate as well as the catalysts. This indicates the involvement of 2 molecules of each in every reaction cycle.

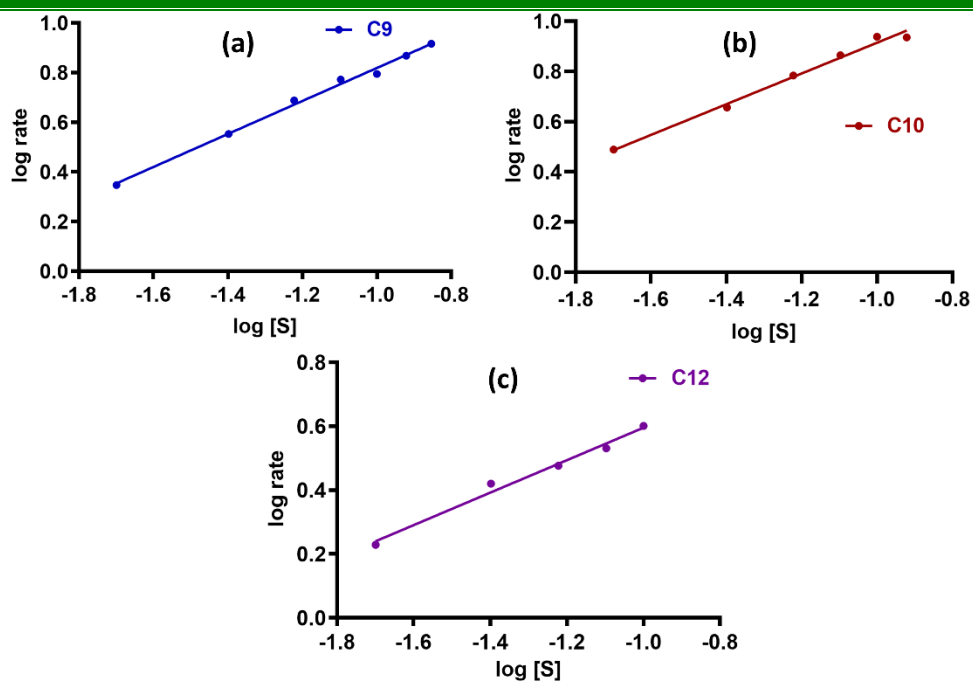


Figure 4.3.4.3 Plot of  $\log(\text{rate})$  vs  $\log[S]$  for complexes (a) C9 (b) C10 and (c) C12

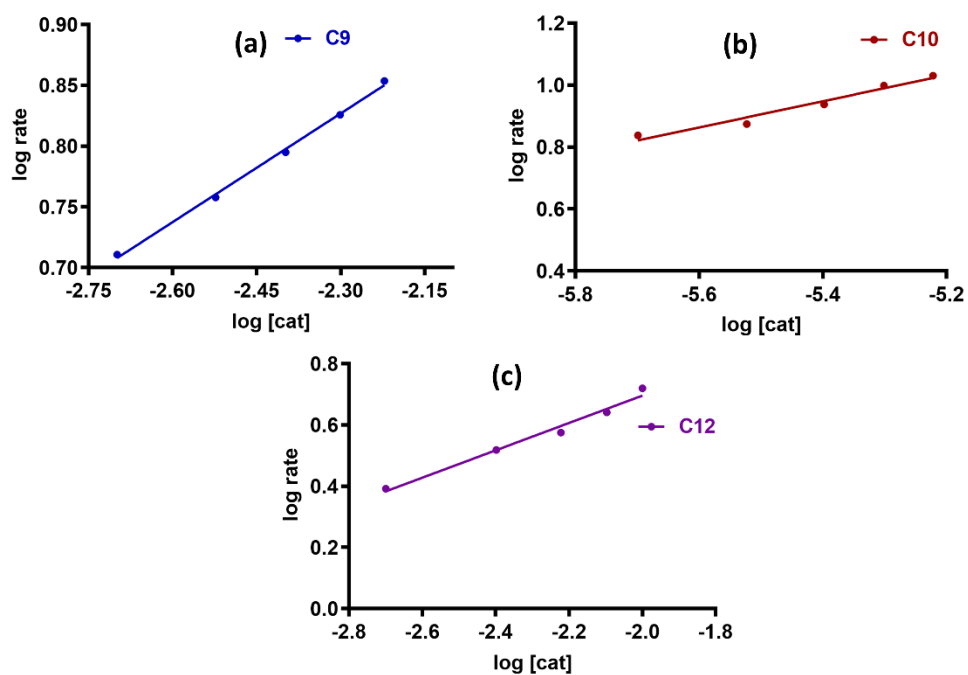


Figure 4.3.4.4 Plot of  $\log(\text{rate})$  vs  $\log[\text{Cat}]$  for complexes (a) C9 (b) C10 and (c) C12

Activation energy of the reaction was found from the Arrhenius plot (**figure 4.3.4.5**). The Activation energy required for the conversion of AA to DHAA is in the range of 27-93 kJ/mole for the complex catalysed reactions.

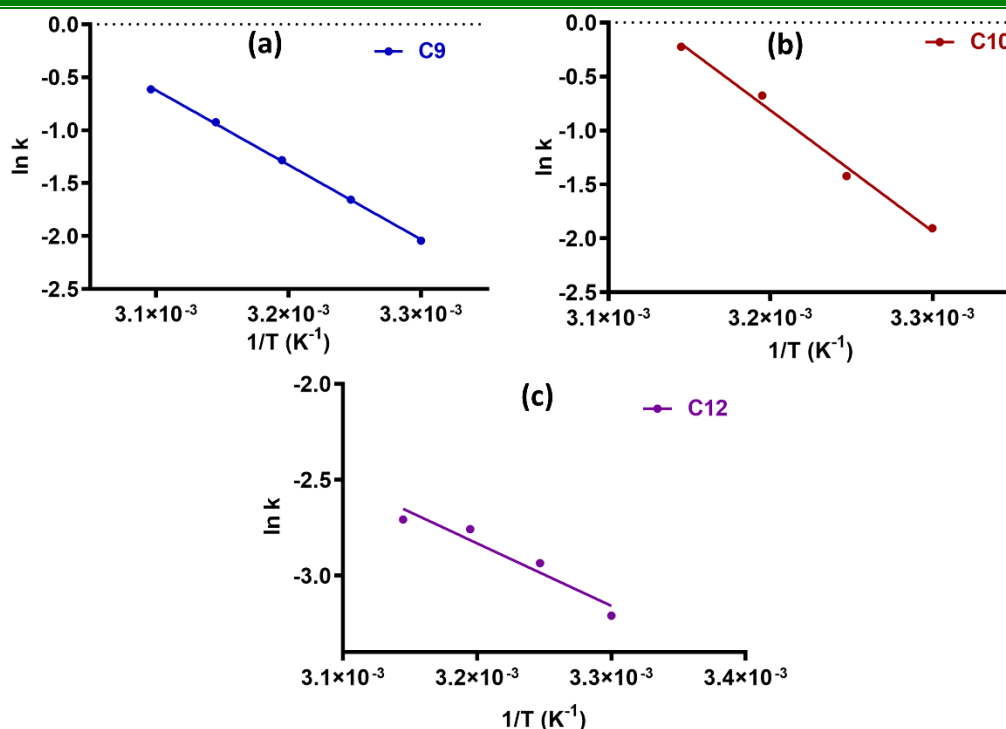


Figure 4.3.4.5 Arrhenius plot of all complexes (a) C9 (b) C10 and (c) C12

The kinetic parameters of AA in the presence of complexes, order and activation energy have been tabulated. (Table 4.3.4.1)

Table 4.3.4.1 Kinetic parameters of AA in presence of complexes, C9, C10 and C12

Complex	$K_m$ (M)	$V_{max}$ ( $\mu\text{M}/\text{min}$ )	$[E]$ (M)	$k_{cat}/h^{-1}$	Order		$E_a$ (kJ/mole)
					Cat	Sub	
C9	$8.19 \times 10^{-5}$	11.56	$4 \times 10^{-6}$	173.4	0.29	0.664	58.462
C10	$6.73 \times 10^{-5}$	13.5		202.5	0.423	0.6119	92.742
C12	$4.45 \times 10^{-2}$	5.395		80.9	0.447	0.508	27.04
AAO <sup>37</sup>	0.08 (mM)	$6.5 (10^4 \text{ mM/s})$		97000	-	-	-
Copper Salt	-	-	-	-	-	-	89.085
No complex	-	-	-	-	-	-	138.99

The presence of any superoxide formed during the reaction was checked spectroscopically and it was found to be absent. The mechanistic pathways of ascorbic acid oxidation may involve production of water or hydrogen peroxide. The formation of hydrogen peroxide was confirmed spectrophotometrically (See SI†: Fig. S4.23) using the literature procedure as explained in Chapter 2 section 2.3.4.<sup>40–42</sup> On the basis

of these observations, the same mechanism as explained in **section 2.3.4** in chapter 2 (**Figure 2.3.4.6**) is considered to be operative in these reactions as well. On the basis of the kinetic parameters, it can be concluded that the complex **C12** is the most active and the activity changes in the order, **C12** > **C9** > **C10**.

#### 4.3.5 Catecholase activity

The studies reported so far on the synthetic tyrosinase and catecholase models typically employ only 3,5-DTBC as a substrate because of its low reduction potential.<sup>43-46</sup> However, there is a lack of literature on the use of other diphenols as substrates and a comparison on the catalytic efficacy of the models with respect to the variations in the nature, electronic character and stereochemistry of substrates.

In the present study, five substrates, 3,5-DTBC, 4-methyl catechol, dopamine, pyrocatechol and 2,3-dihydroxy naphthalene have been employed to study the catecholase activity of the complexes. The reaction with pyrocatechol and 2,3-dihydroxy naphthalene was found to be very slow. The corresponding quinone band in pyrocatechol and 2,3-dihydroxy naphthalene had negligible appearance even after 24 hrs of reaction time indicating negligible catalytic activity of the complex for these two substrates. The complex **C9** was found to be active with dopamine and other complexes were found to be inactive with negligible appearance of quinone band even after 24 hrs indicating no catalytic activity with complexes **C10** and **C12** as catalysts for oxidation of dopamine. All complexes were found to be active for the oxidation of 3,5-DTBC and 4-methyl catechol as substrates. Further detailed kinetic studies were carried out with 3,5-DTBC and 4-methylcatechol as explained in **section 2.3.5** in Chapter 2. The course of a typical reaction of 3,5-DTBC oxidation with solution of complex **C9** (**Figure 4.3.5.1 (a)**) and for other complexes and substrates (see SI† in **Fig 4.17A-B(a)** and **4.18A-B(a)** inset graph) was followed spectrophotometrically. The substrate 3,5-DTBC / 4-methyl catechol was added at once to the solution of the complex and the spectra were recorded. A new band corresponding to 3,5-DTBQ / 4-methyl quinone started appearing at 380–410 nm. A linear increase in the absorption of this band was monitored. The kinetics of oxidation of 3,5-DTBC and 4-methyl catechol was determined by the method of initial rates as a function of time (**figure 4.3.5.1 (b-d)** for **C9** (3,5-DTBC)). (See SI† **Fig. 4.17-4.18(b-d)** for other complexes and substrates).

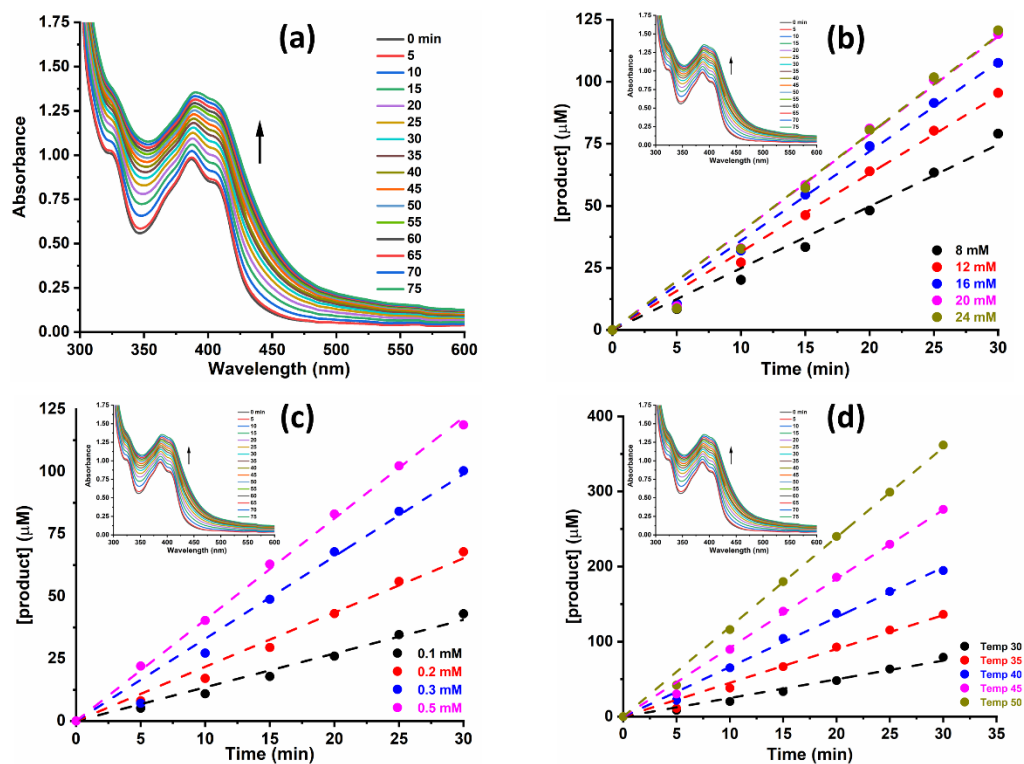


**Figure 4.3.5.1** (a) Time dependent spectral changes over a time period of 0-30min in 3,5-DTBC corresponding to **C9** catalyzed oxidation and (b-d) Plot of [product] as function of time with respect to substrate (b), catalyst (c) and temperature (d) (Inset: Plot of absorbance vs wavelength at different time interval) for complex **C9** with 3,5-DTBC

The analysis of the data based on the Michaelis-Menten model, originally developed for enzyme kinetics, was applied. The solid circles are experimental data and the solid curves are the fits to the Michaelis-Menten model for all complexes with 3,5-DTBC (**figure 4.3.5.2 (a-b)**) and that of complex **C9** with Dopamine (**figure 4.3.5.3(a)**) (for 4-MC see SI† **Fig S4.19**). With various concentrations of substrates, Michaelis-Menten constant ( $K_m$ ) can be obtained from the Michaelis-Menten equation. The Lineweaver-Burk plot for all complexes with 3,5-DTBC are depicted in inset of **figure 4.3.5.2 (a-b)** and for complex **C9** with dopamine are depicted in **figure 4.3.5.3(a)** (Inset) while those for 4-MC are given in SI† Fig. S4.19 Inset.

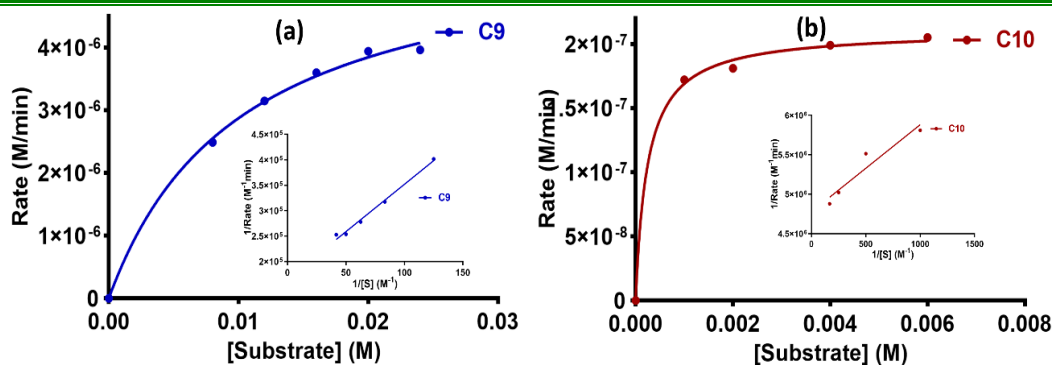


**Figure 4.3.5.2** Plot of Rate vs [Substrate] of Michaelis Menten model for complexes (a) **C9** and (b) **C10** (Inset: Lineweaver Burk plot) for 3,5-DTBC

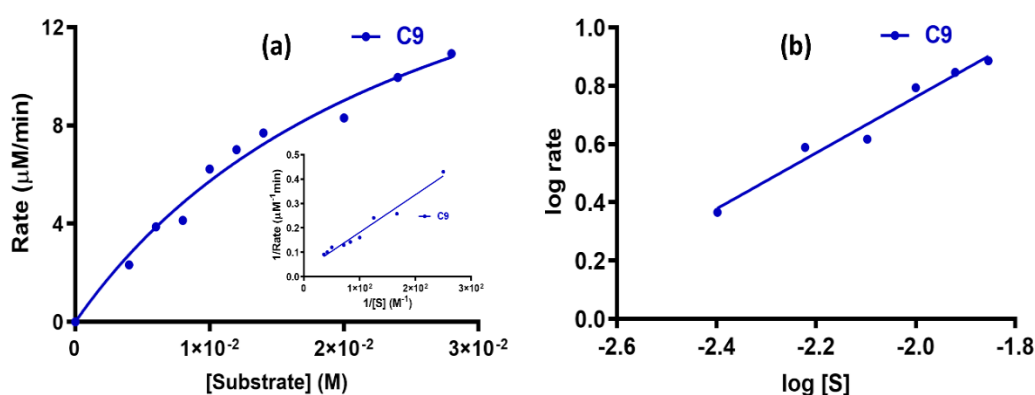


**Figure 4.3.5.3** (a) Plot of Rate vs [Substrate] of Michaelis Menten model for complex **C9** (Inset: Lineweaver Burk plot) for Dopamine (b) Plot of log rate vs log [Sub] for complex **C9** for Dopamine

The plots of log (rate) versus log[substrate] (**Figure 4.3.5.4 (a-b)**) and log (rate) versus log[catalyst] for 3,5-DTBC with all complexes (**Figure 4.3.5.5 (a-b)**) and those for 4-MC (SI† **Fig. 4.20, 4.21**) and dopamine (**Figure 4.3.5.3(a)** and **Figure 4.3.5.6(a)**) indicate that the complex catalysed oxidation of both diphenols to the corresponding quinones follow first order kinetics with respect to the substrate and also with respect to the dicopper(II) monomer of the complexes.

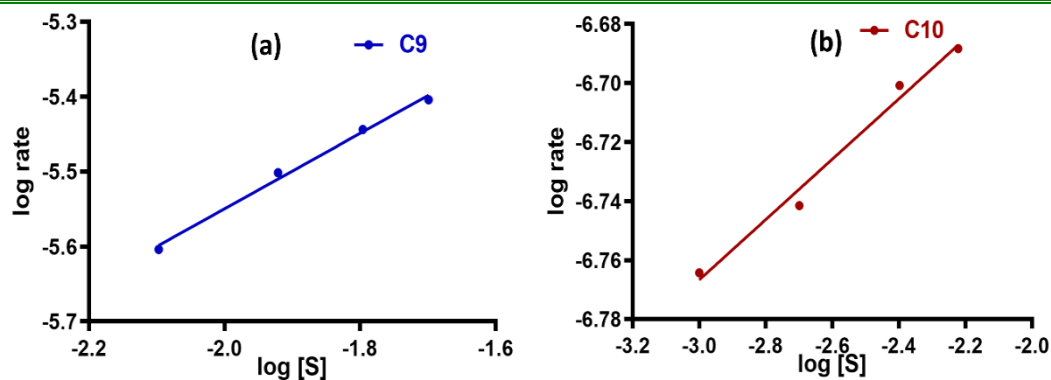


Figure 4.3.5.4 Plot of log rate vs log [Sub] for complexes (a) C9 and (b) C10 for 3,5-DTBC

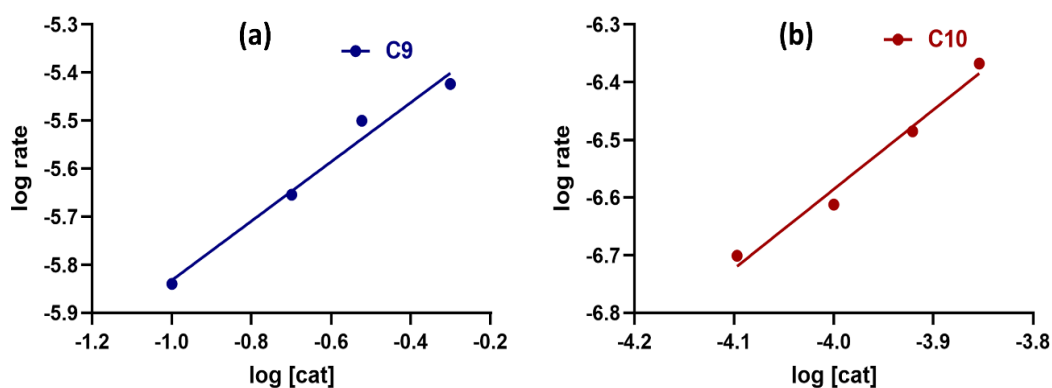


Figure 4.3.5.5 Plot of log rate vs log [Cat] for complexes (a) C9 and (b) C10 for 3,5-DTBC

The activation energy values for the oxidation of various substrates in presence of the complex catalysts have been calculated from Arrhenius plot (Figure 4.3.5.5 (a-b), SI† Fig. S4.23 and SI I† Figure 4.3.5.6 (b)).

The kinetic parameters, order of reaction with respect to the catalyst as well as substrate and activation energy listed in Table 4.3.5.1.

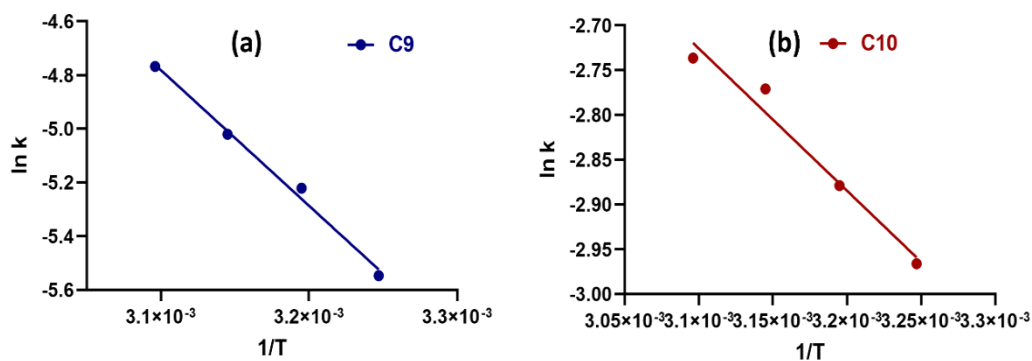
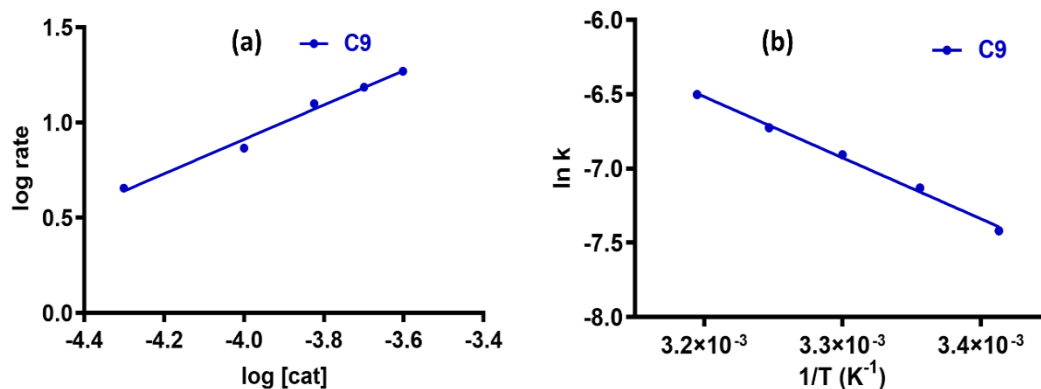


Figure 4.3.5.5 Arrhenius plot of all complexes (a) C9 and (b) C10 for 3,5-DTBC



**Figure 4.3.5.6** (a) Plot of log rate vs log [cat] for complex **C9** and (b) Arrhenius plot of complex **C9** for Dopamine

**Table 4.3.5.1** Kinetic parameters of Michaelis Menten model, Order, Activation energy of substrates with **C9** and **C10** complexes

Complexes	Substrate	$V_{\max}$ (M/s)	$K_m$ (M)	$k_{\text{cat}}$ ( $\text{h}^{-1}$ )	Order		$E_a$ (kJ/mol e)
					Cat	Sub	
<b>C9</b>	3,5-DTBC	$9.68 \times 10^{-8}$	$1.02 \times 10^{-2}$	5.81	0.702	0.50	42.01
	4-MC	$1.74 \times 10^{-7}$	$3.56 \times 10^{-2}$	18.7	0.9367	0.665	17.18
	Dopamine	$3.52 \times 10^{-7}$	$2.69 \times 10^{-1}$	63.4	0.9029	0.9593	34.16
<b>C10</b>	3,5-DTBC	$2.10 \times 10^{-7}$	$2.47 \times 10^{-4}$	94.5	1.377	0.159	26.26
	4-MC	$5.63 \times 10^{-8}$	$9.78 \times 10^{-2}$	24.3	1.09	0.7503	37.66

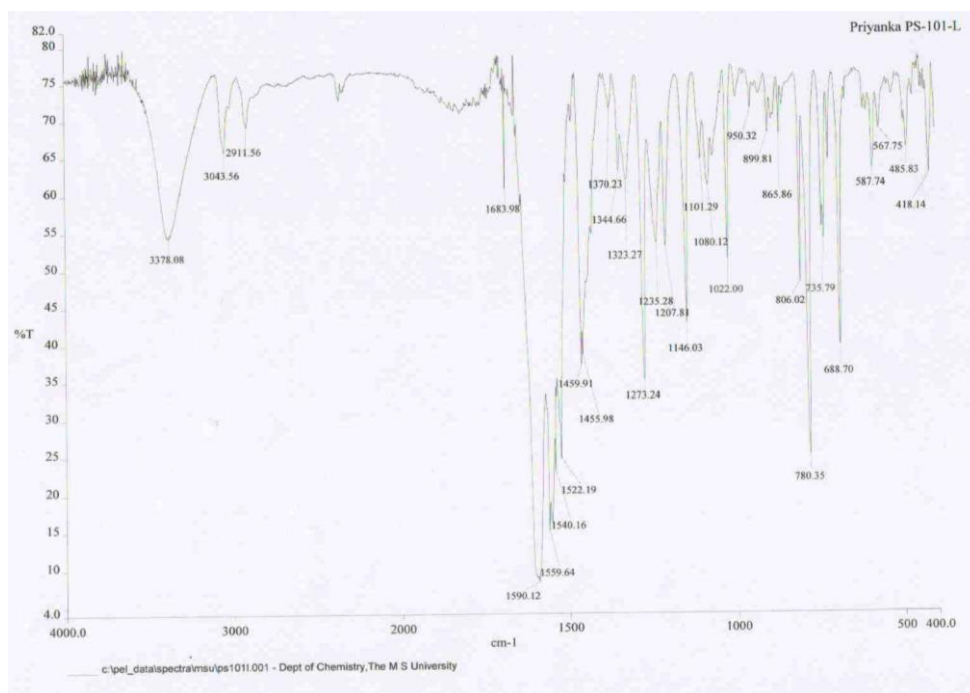
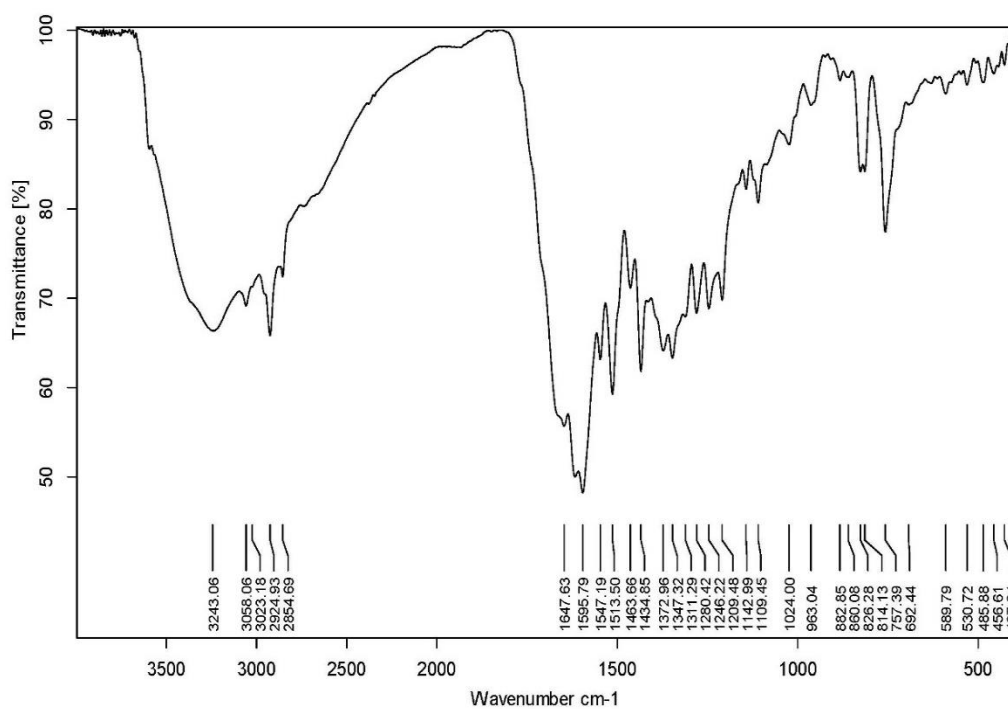
It can be seen from the values in **Table 4.3.5.1** that the isomeric complexes, **C9** and **C10** have altogether different activity and selectivity towards different substrates. **C9** behaves as a very efficient catalyst for the oxidation of dopamine whereas **C10** is totally inactive. Both complexes are efficient catalysts for the oxidation of 3,5-DTBC and 4-MC, however, **C9** is more active for 4-MC whereas **C10** is more active for the oxidation of 3,5-DTBC. This difference in the selectivity can be attributed to the variation in electron at the coordinating sites and the steric factors which might be influencing the recognition of the substrates by the active sites. The presence of any superoxide formed during the reaction was checked spectroscopically and it was found to be absent. The mechanistic pathways of catechol oxidation may involve production of water or hydrogen peroxide. The formation of hydrogen peroxide was confirmed spectrophotometrically (See SI†: **Fig. S.4.23**) using a literature procedure as explained in Chapter 2 **section 2.3.4**.<sup>40–42</sup> . On the basis of these observations, the same mechanism as explained in **section 2.3.4** in chapter 2 (**Figure 2.3.5.5**) is considered to be operative in these reactions as well.

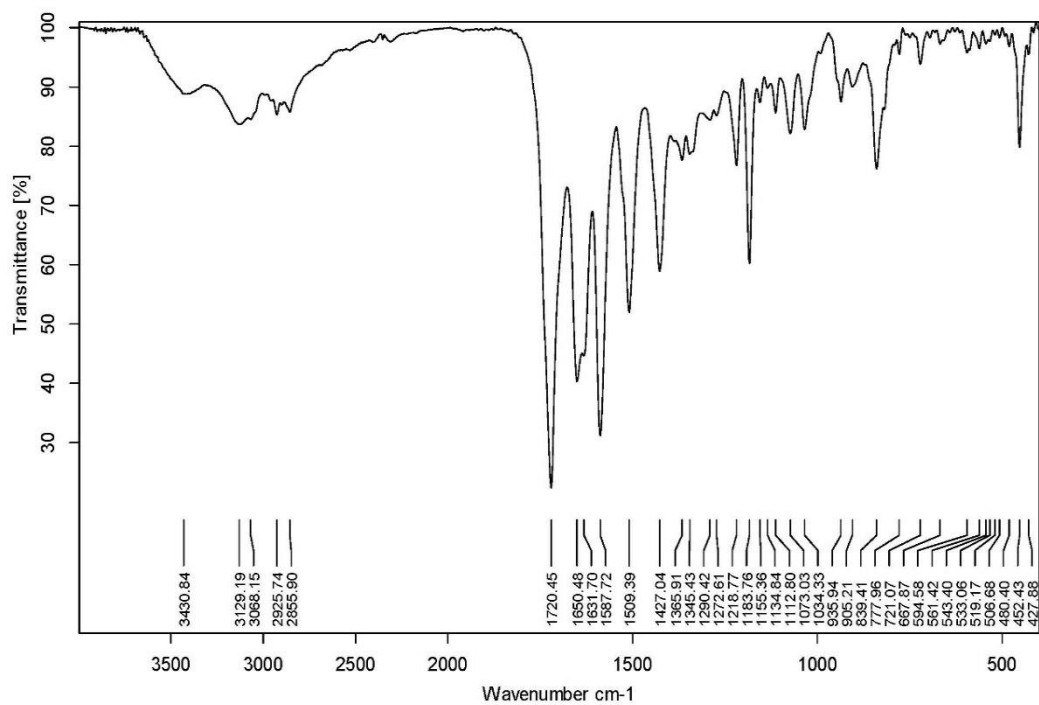
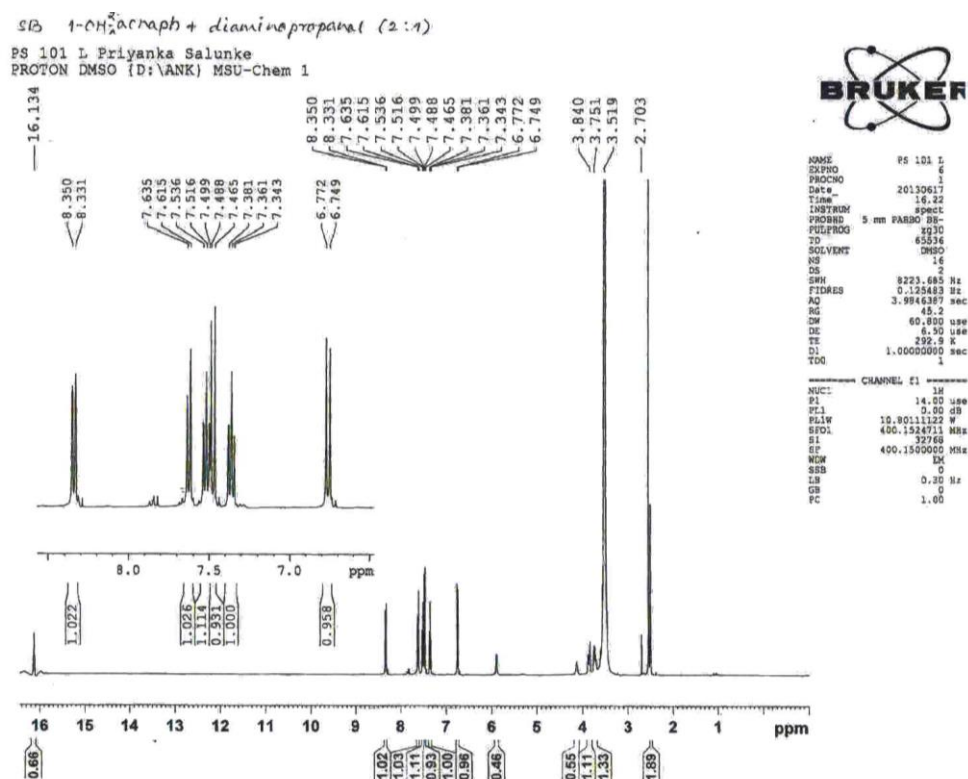
---

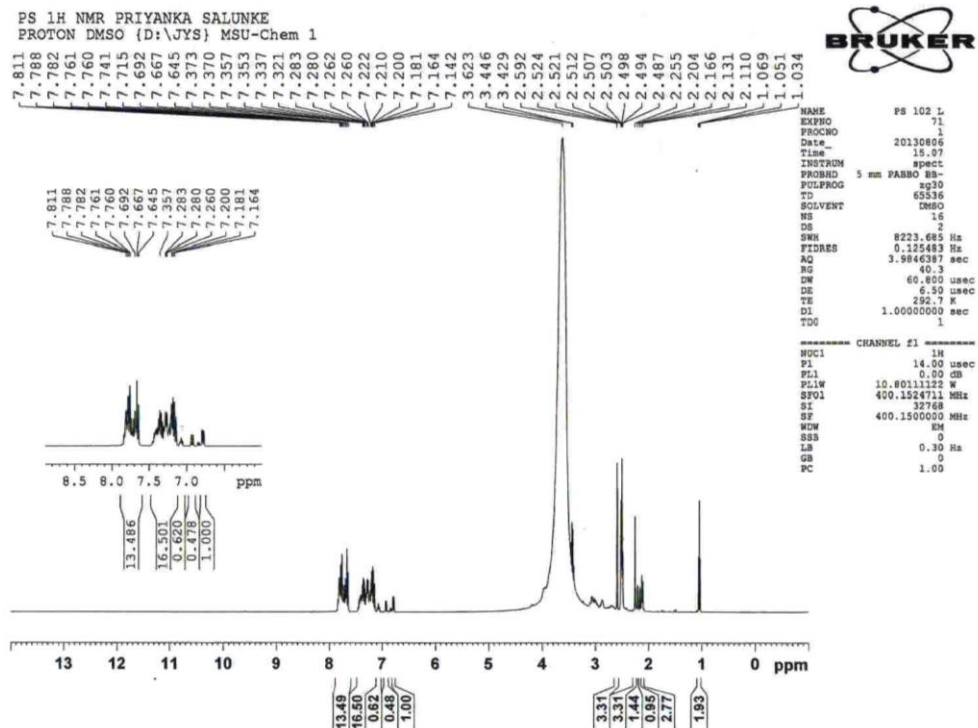
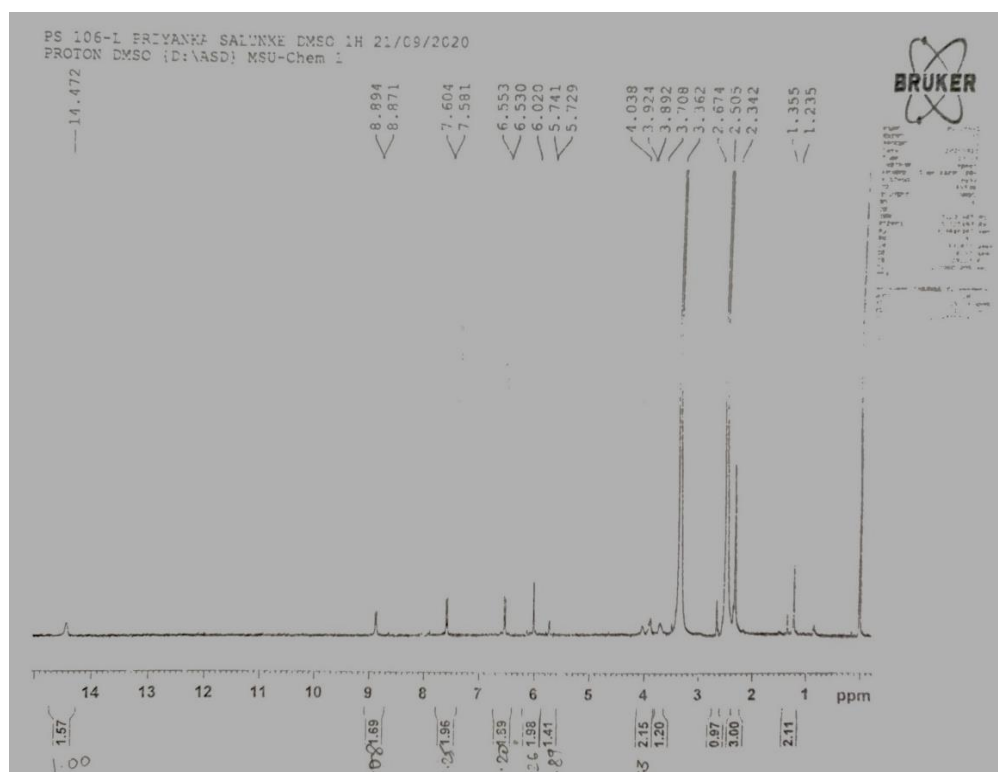
## 4.4 CONCLUSION

- Synthesis and characterisation of three new compartmental Schiff bases of aldehydes and naphthones (**L<sup>9</sup>**, **L<sup>10</sup>** and **L<sup>12</sup>**) and their dicopper(II) complexes (**C9**, **C10** and **C12**) has been carried out.
- The complexes possess moderate antiferromagnetism.
- Kinetics of Ascorbic acid oxidase activity of dicopper(II) complexes with ascorbic acid as substrate has been studied under aerobic conditions and by varying parameters like concentration of substrate and catalyst and temperature. Complex **C10** has high ascorbic acid oxidase activity over other complexes in the following order: **C10** ≥ **C9** > **C12**.
- SOD mimic activity of dicopper(II) complexes has been studied. Complex **C9** has significantly high SOD mimic activity over other complexes in the following order: **C9** > **C10** > **C12**.
- Kinetics of catecholase activity of the dicopper(II) complexes with 3,5-DTBC and 4-methyl catechol and dopamine has been studied by varying parameters like concentration of substrate and catalyst and temperature. Complex **C10** has better catecholase activity for 3,5-DTBC while **C9** is more active for 4-methyl catechol. Complex **C9** selectively binds with dopamine and oxidizes it while complex **C10** is inactive. This shows its selectivity towards substrate. Complex **C12** has found to be less active.

## Supplementary Information

Fig. S4.1 IR spectrum of  $L^9$ Fig. S4.2 IR spectrum of  $L^{10}$

Fig. S4.3 IR spectrum of  $L^{12}$ Fig. S4.4  $^1\text{H}$  NMR spectrum of  $L^9$

Fig. S4.5  $^1\text{H}$  NMR spectrum of  $\text{L}^{10}$ Fig. S4.6  $^1\text{H}$  NMR spectrum of  $\text{L}^{12}$

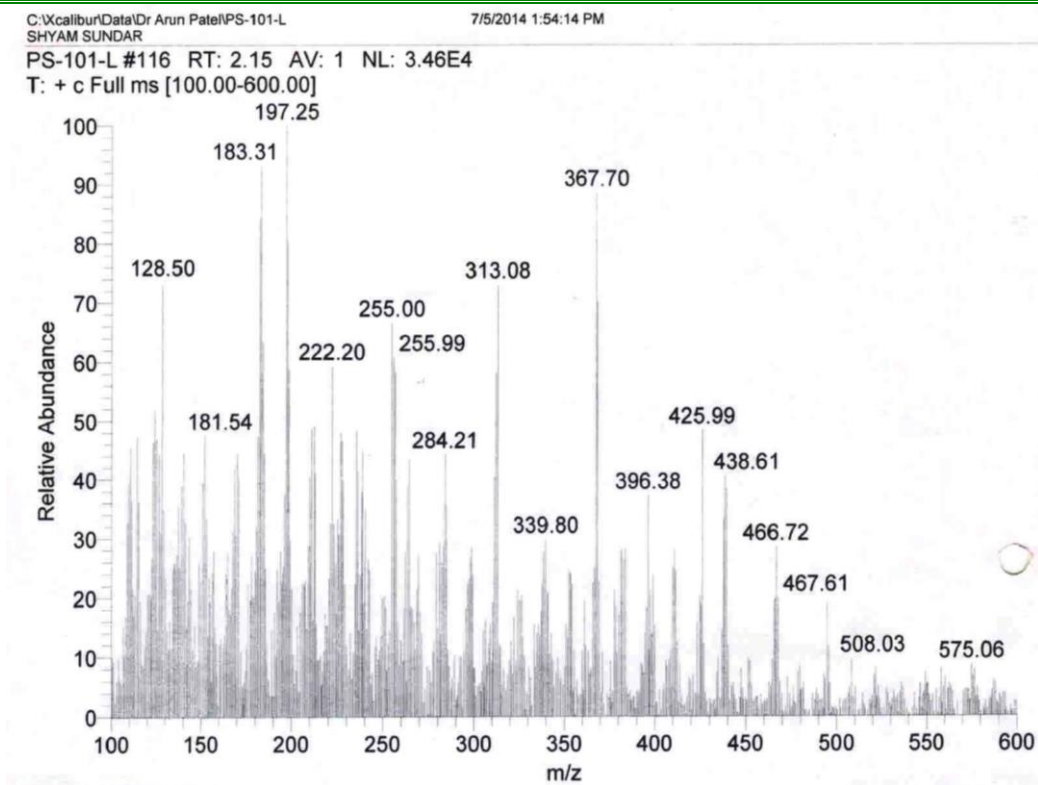


Fig. S4.7 Mass spectrum of  $L^9$

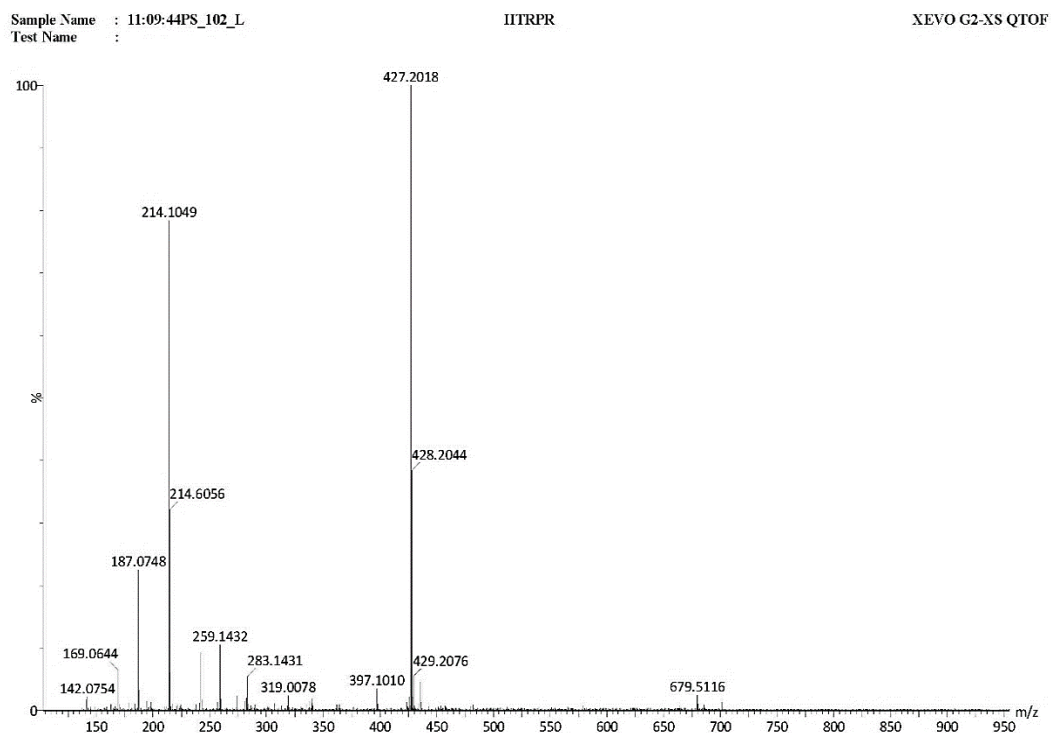


Fig. S4.8 Mass spectrum of  $L^{10}$

Sample Name : 11:12:27PS\_106\_L  
Test Name :

IITRPR

XEVO G2-XS QTOF

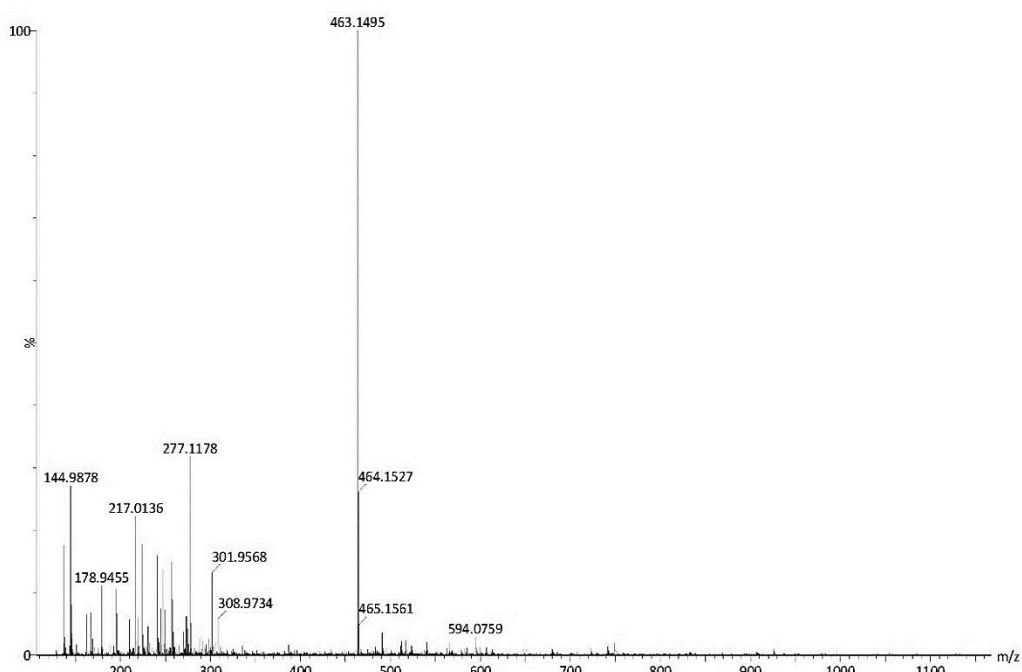


Fig. S4.9 Mass spectrum of  $L^{12}$

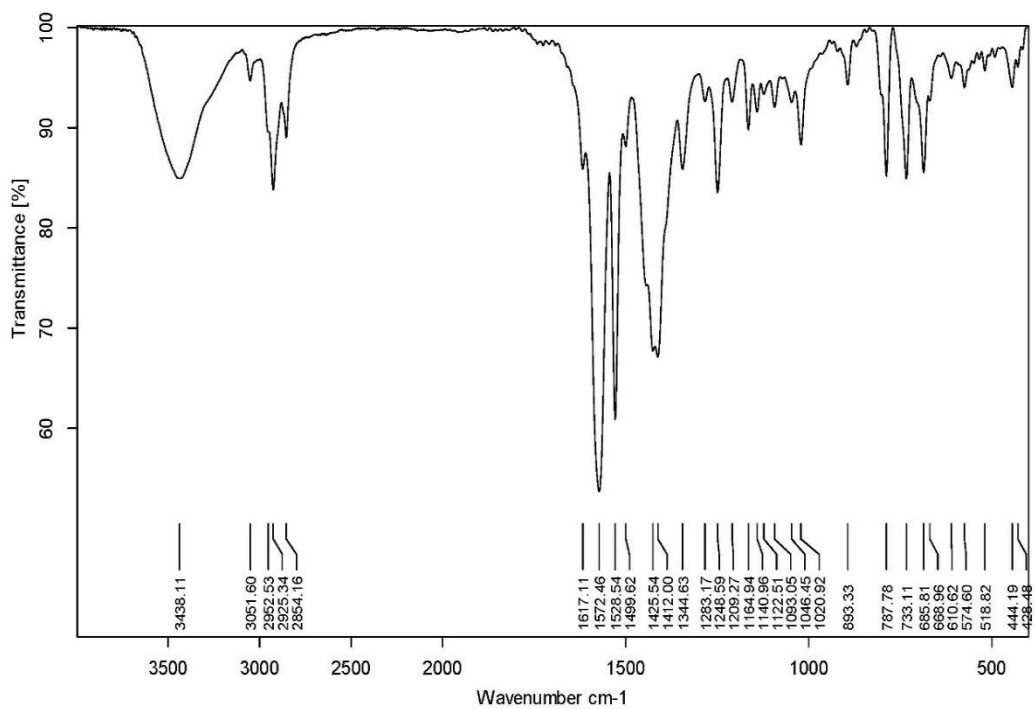


Fig. S4.10 IR spectrum of complex  $C9$

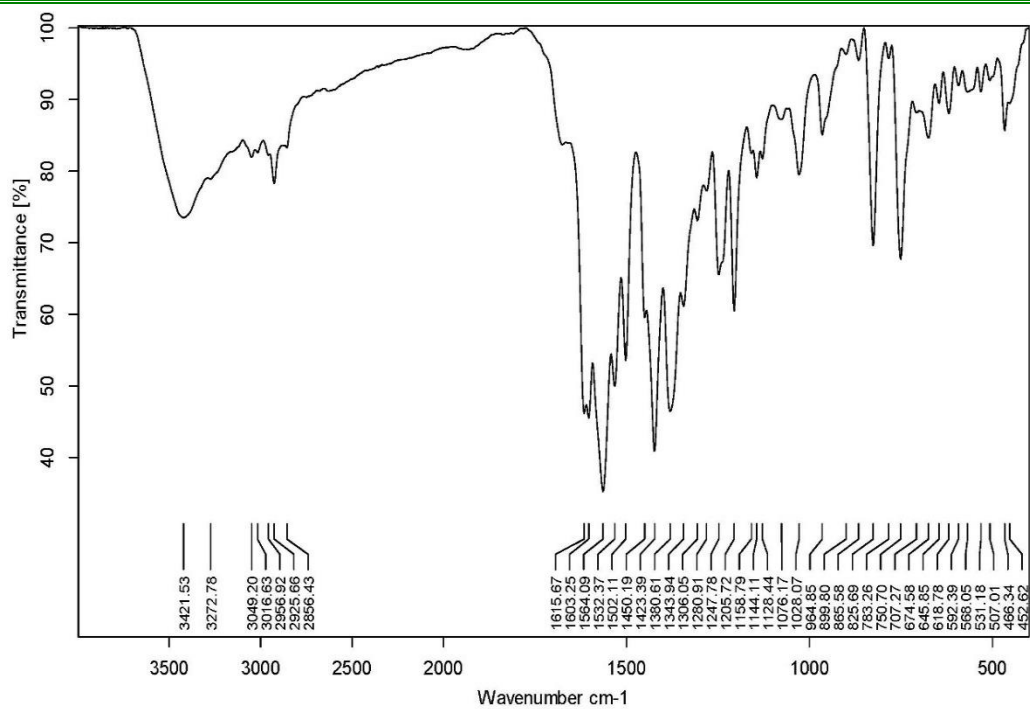


Fig. S4.11 IR spectrum of complex C10

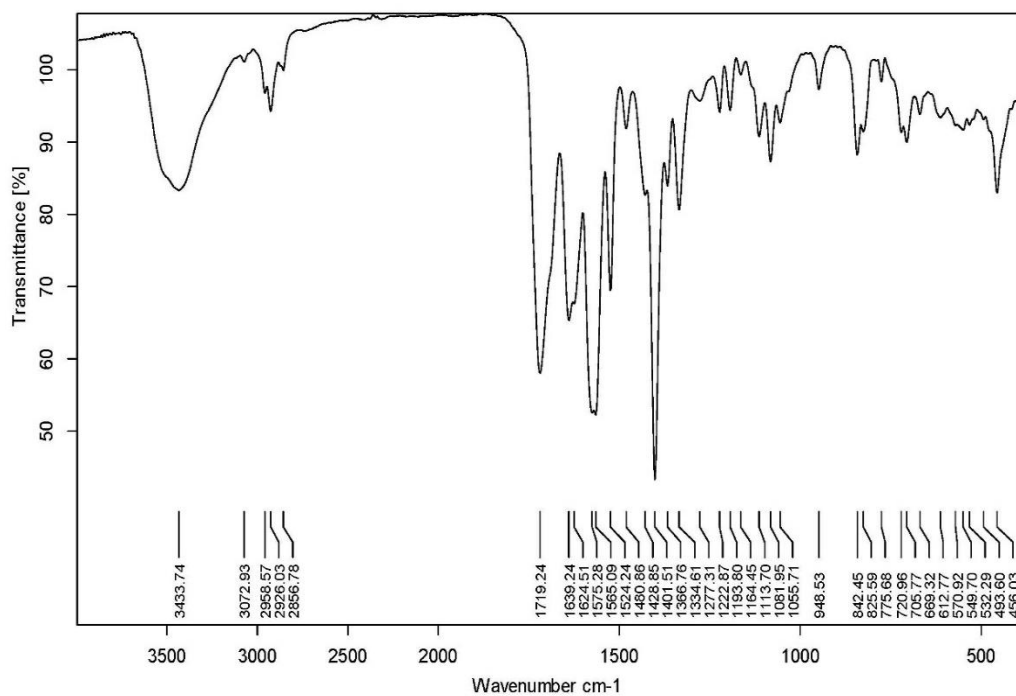
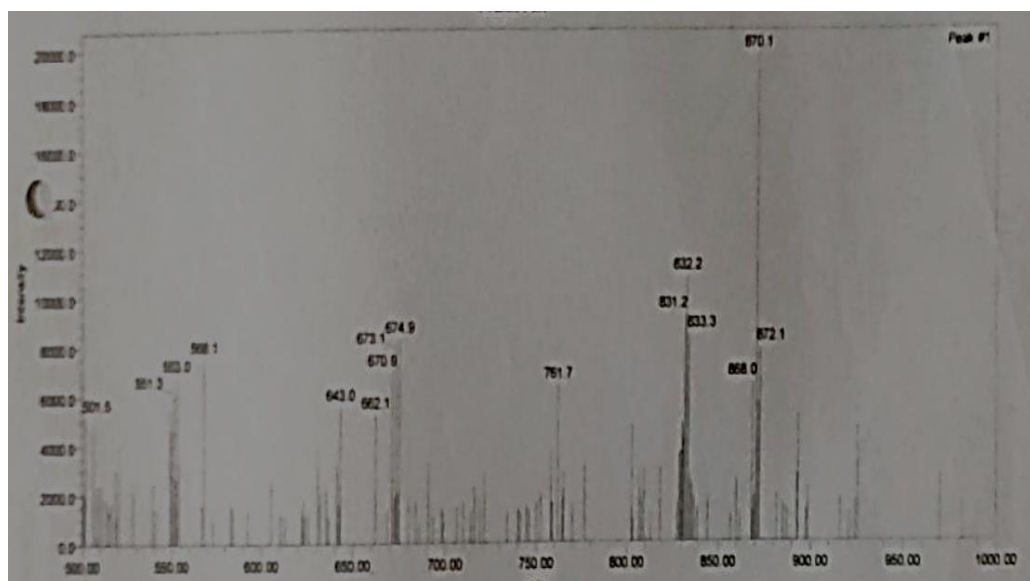
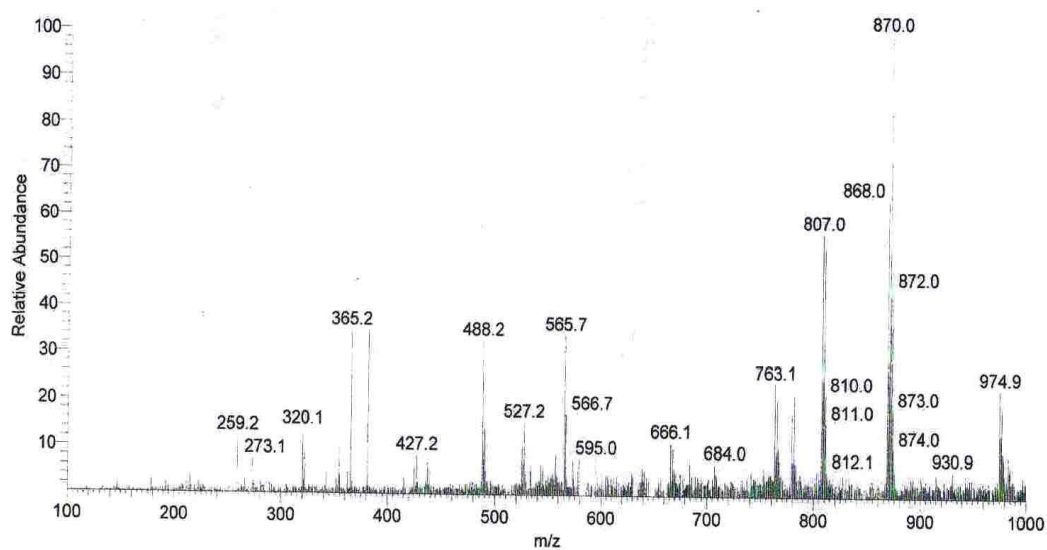


Fig. S4.12 IR spectrum of complex C12



*Fig. S4.13* Mass spectrum of complex C9



*Fig. S4.14* Mass spectrum of complex C10

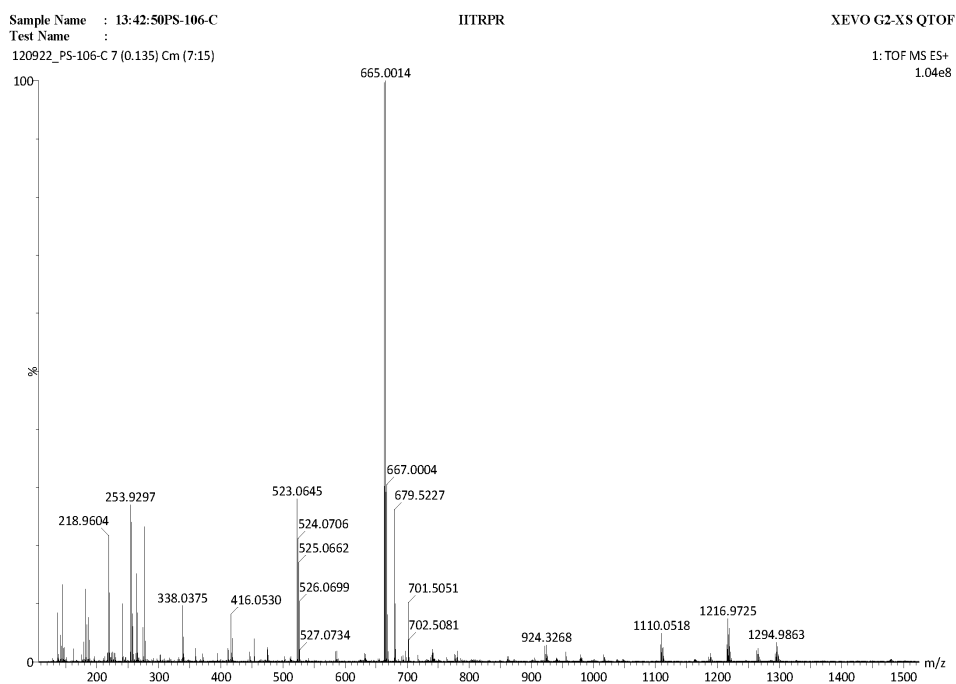


*Fig. S4.15* Mass spectra of complex *C12*

*Table S4.1* Calculated bond parameters of complex *C9*

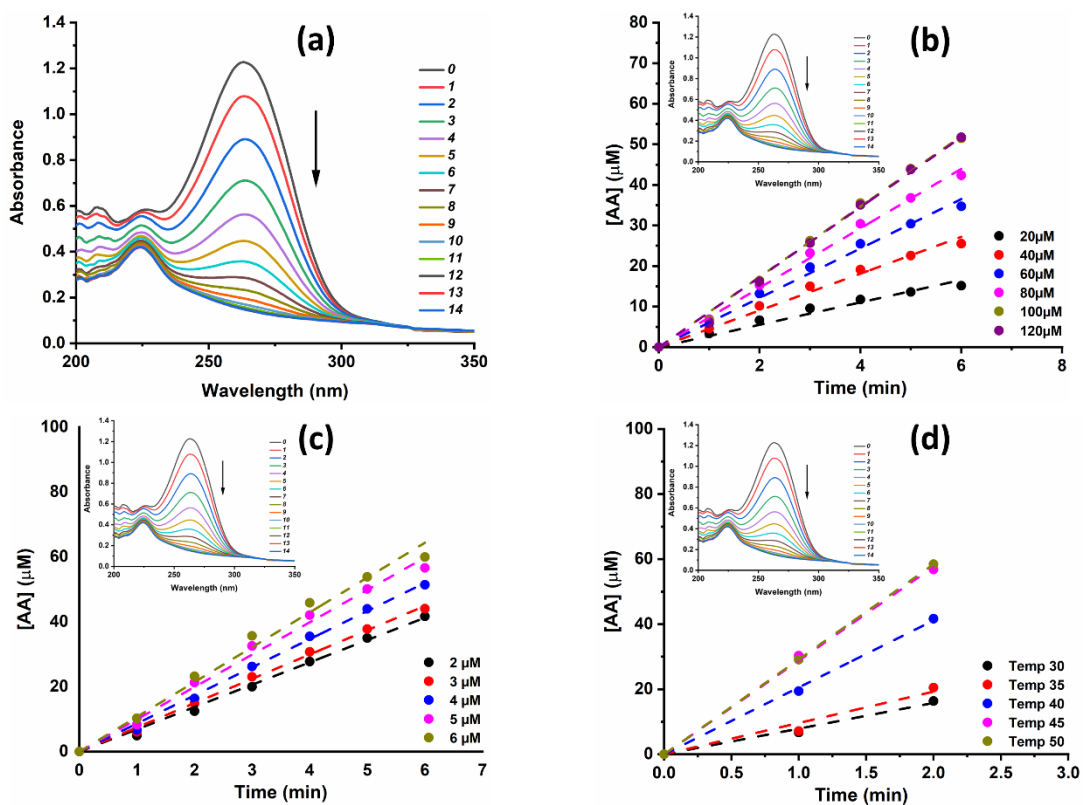
<i>C9</i>		
<b>Cu-N Distances (Å<sup>o</sup>)</b>		
R(9,56)	N9-Cu56	1.9566
R(4,57)	N4-Cu57	1.9566
<b>Cu-O Distances (Å<sup>o</sup>)</b>		
R(7,56)	O7-Cu56	1.9432
R(7,57)	O7-Cu57	1.9432
R(35,56)	O35-Cu56	1.9393
R(29,57)	O29-Cu57	1.9392
R(63,56)	O63-Cu56	1.9688
R(64,57)	O64-Cu57	1.9691
<b>Bond angles</b>		
A(7,56,9)	O7-Cu56-N9	86.6525
A(7,56,63)	O7-Cu56-O63	91.6532
A(9,56,35)	N9-Cu56-O35	92.0173
A(35,56,63)	O35-Cu56-O63	89.7278
A(4,57,7)	N4-Cu57-O7	86.6494
A(4,57,29)	N4-Cu57-O29	92.0311
A(7,57,64)	O7-Cu57-O64	91.6413
A(29,57,64)	O29-Cu57-O64	89.7299

Table S4.1 (Contd...) Calculated bond parameters of complex C10

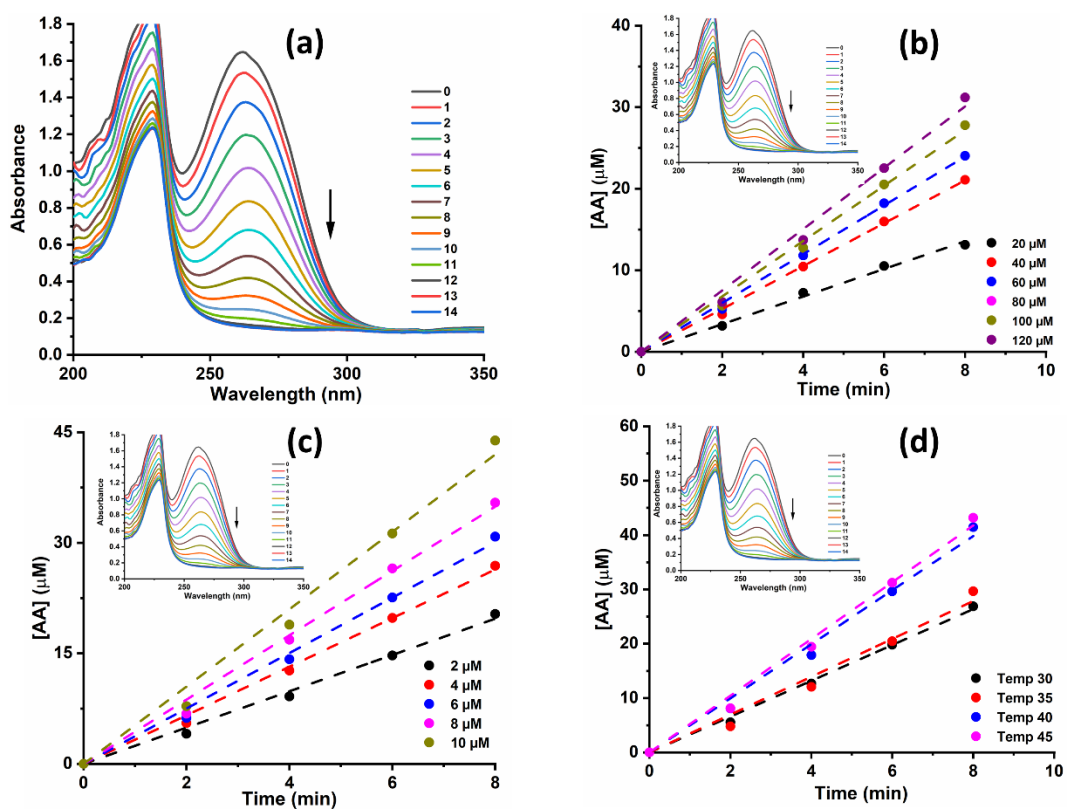
<b>C10</b>		
<b>Cu-O Distances (Å)</b>		
R(29,63)	O29-Cu63	1.9653
R(30,64)	O30-Cu64	1.9646
R(23,63)	O23-Cu63	1.9452
R(22,64)	O22-Cu64	1.9501
R(7,63)	O7-Cu63	1.9339
R(7,64)	O7-Cu64	1.9402
<b>Bond angles</b>		
A(7,63,9)	O7-Cu63-N9	85.7767
A(7,63,29)	O7-Cu63-O29	92.2376
A(9,63,23)	N9-Cu63-N23	90.1219
A(23,63,29)	O23-Cu63-N29	92.4415
A(4,64,7)	N4-Cu64-O7	86.3787
A(4,64,22)	N4-Cu64-O22	90.5748
A(7,64,30)	O7-Cu64-O30	92.6065
A(22,64,30)	O22-Cu64-O30	95.5983
<b>Torsional angles</b>		
L(7,63,23,29,-1)	O7-Cu63-O23-O29 (-1)	184.679
L(9,63,29,23,-1)	N9-Cu63-O29-O23 (-1)	182.5634
L(4,64,30,7,-1)	N4-Cu64-O30-O7 (-1)	178.9852
L(7,63,23,29,-2)	O7-Cu63-O23-O29 (-2)	189.1697
L(9,63,29,23,-2)	N9-Cu63-O29-O23 (-2)	183.3624
L(4,64,30,7,-2)	N4-Cu64-O30-O7 (-2)	166.0257

Table S4.1 (Contd..) Calculated bond parameters of complex C12

C12		
<b>Cu-N Distances (Å°)</b>		
R(13,47)	N13-Cu46	1.9395
R(14,46)	N14-Cu47	1.9395
<b>Cu-O Distances (Å°)</b>		
R(53,46)	O53-Cu46	1.9525
R(54,47)	O54-Cu47	1.9527
R(39,46)	O39-Cu46	1.9527
R(39,47)	O39-Cu47	1.9525
R(40,46)	O40-Cu46	1.9694
R(41,47)	O41-Cu47	1.9693
<b>Bond angles</b>		
A(14,46,39)	O7-Cu63-N9	84.9936
A(14,46,40)	O7-Cu63-O29	92.3958
A(39,46,53)	N9-Cu63-N23	92.5377
A(40,46,53)	O23-Cu63-N29	91.0713
A(13,47,39)	N4- Cu64-O7	84.9927
A(13,47,41)	N4-Cu64-O22	92.3978
A(39,47,54)	O7-Cu64-O30	92.5465
A(41,47,54)	O22-Cu64-O30	91.0574
<b>Torsional angles</b>		
L(14,46,53,40,-1)	N14-Cu46-O53-O40 (-1)	183.4671
L(39,46,40,53,-1)	O39-Cu46-O40-O53 (-1)	183.609
L(13,47,54,41,-1)	N13-Cu47-O54-O41 (-1)	183.4552
L(39,47,41,54,-1)	O39-Cu47-O41-O54 (-2)	183.6039
L(14,46,53,40,-2)	N14-Cu46-O53-O40 (-2)	186.6848
L(39,46,40,53,-2)	O39-Cu46-O40-O53 (-2)	188.0746
L(13,47,54,41,-2)	N13-Cu47-O54-O41 (-2)	173.3307
L(39,47,41,54,-2)	O39-Cu47-O41-O54 (-2)	171.9381



**Fig. S4.16A** (a) Time dependent spectral changes from 0 to 14 mins of AA corresponding to **C10** catalyzed oxidation and (c-e) Plot of  $[AA]$  as function of time with respect to. substrate (c), catalyst (d) and temperature (e) (Inset: Plot of absorbance vs wavelength at different time interval) with AA



*Fig. S4.16B (a) Time dependent spectral changes from 0 to 14 mins of AA corresponding to C12 catalyzed oxidation and (c-e) Plot of [AA] as function of time with respect to substrate (c), catalyst (d) and temperature (e) (Inset: Plot of absorbance vs wavelength at different time interval)*

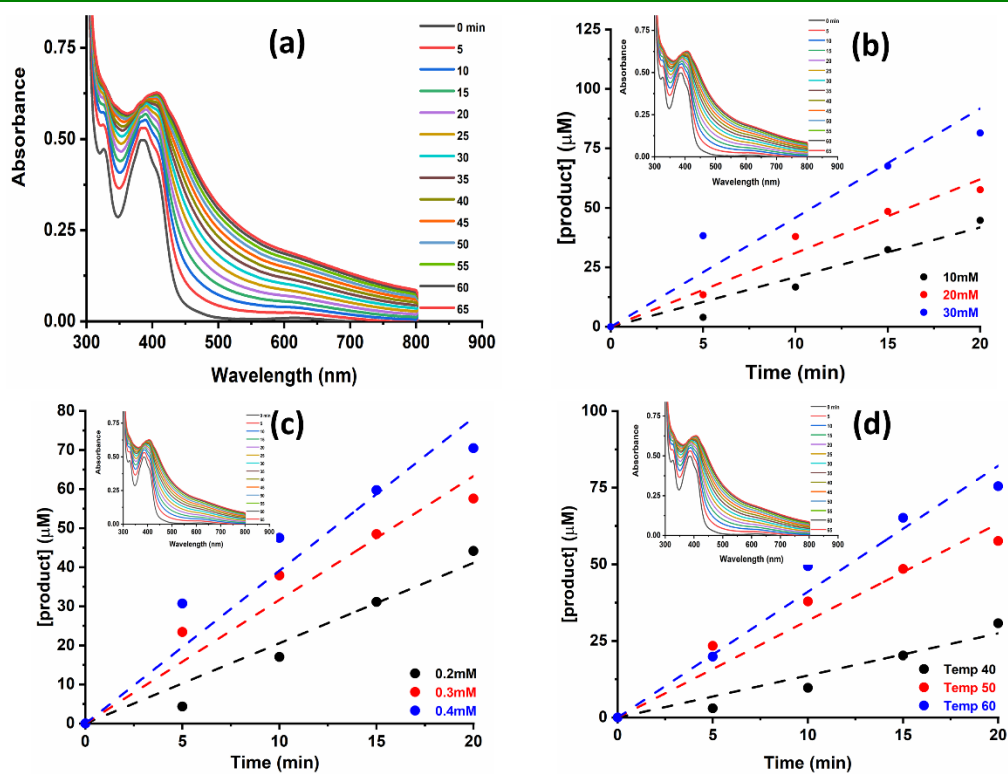


*Fig. S4.17A (a) Time dependent spectral changes over a time period of 4-MC corresponding to C9 catalyzed oxidation and (b-d) Plot of [product] as function of time with respect to substrate (b), catalyst (c) and temperature (d) (Inset: Plot of absorbance vs wavelength at different time interval) for complex C9 with 4-MC*

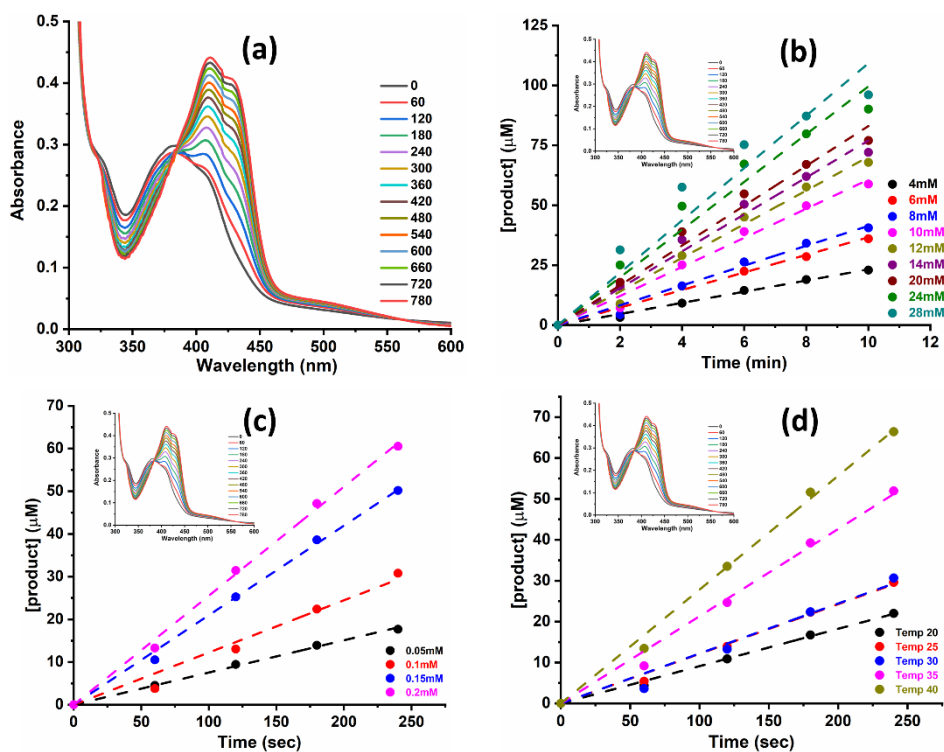


**Fig. S4.17B** (a) Time dependent spectral changes over a time period of Dopamine corresponding to C9 catalyzed oxidation and (b-d) Plot of [product] as function of time with respect to substrate (b), catalyst (c) and temperature (d) (Inset: Plot of absorbance vs wavelength at different time interval) for complex C9 with Dopamine

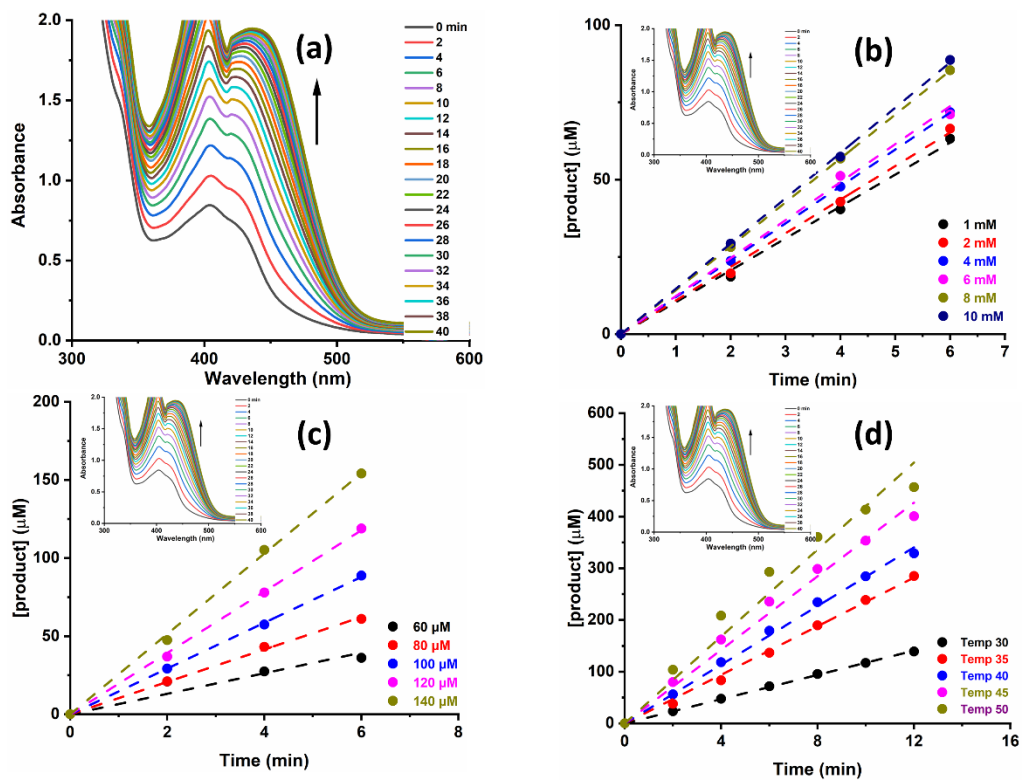


**Fig. S4.18A** (a) Time dependent spectral changes over a time period of 3,5-DTBC corresponding to  $C10$  catalyzed oxidation and (b-d) Plot of [product] as function of time with respect to substrate (b), catalyst (c) and temperature (d) (Inset: Plot of absorbance vs wavelength at different time interval) for complex  $C10$  with 4-MC

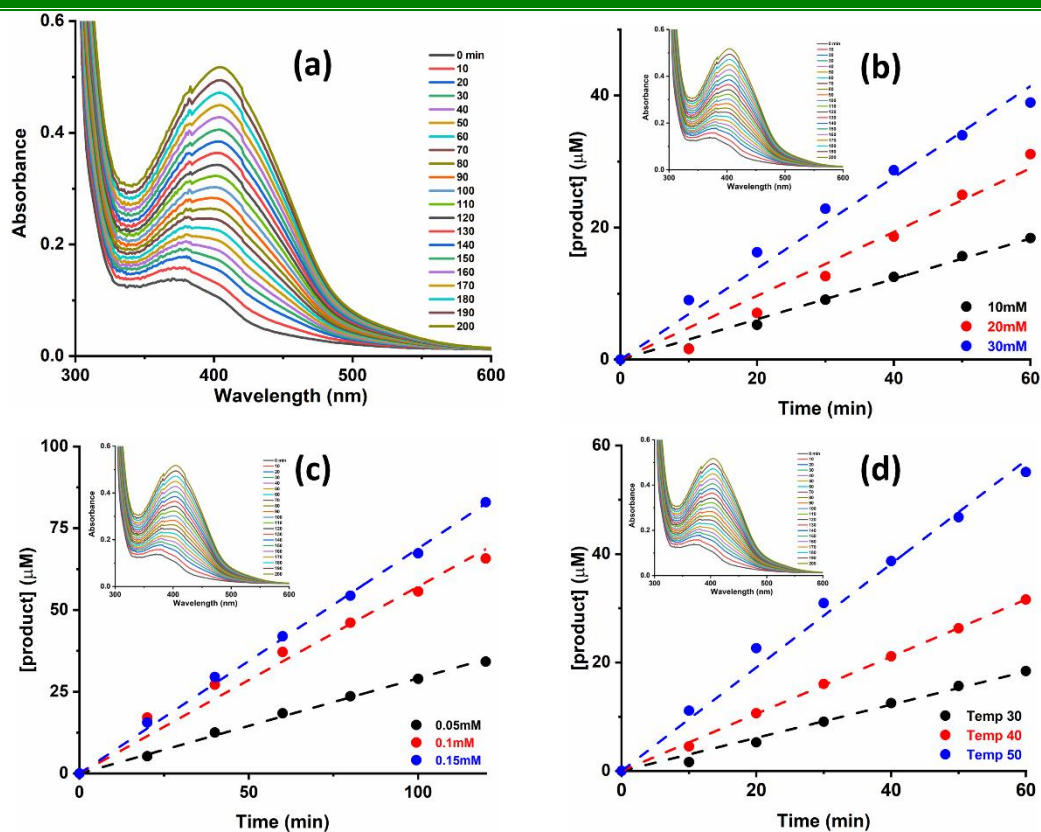


**Fig. S4.18B** (a) Time dependent spectral changes over a time period of 4-MC corresponding to C10 catalyzed oxidation and (b-d) Plot of [product] as function of time with respect to substrate (b), catalyst (c) and temperature (d) (Inset: Plot of absorbance vs wavelength at different time interval) for complex C10 with 4-MC

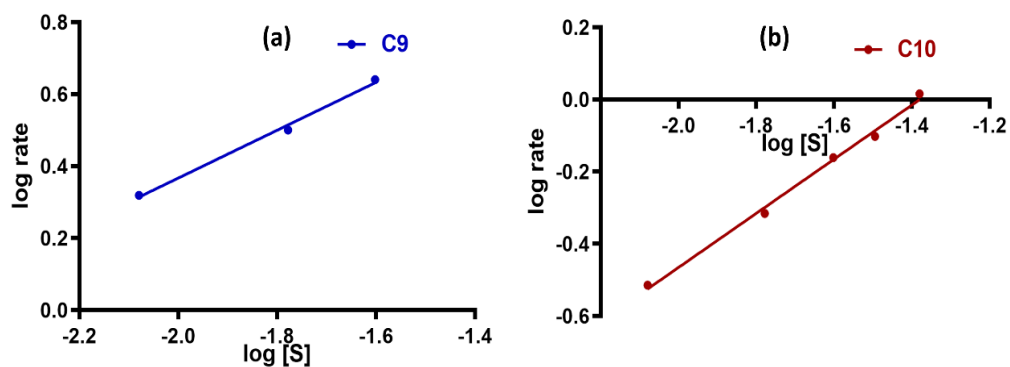


**Fig. S4.19** Plot of Rate vs [Substrate] of Michaelis Menten model for complexes (a) C9 and (b) C10 (Inset: Lineweaver Burk plot) for 4-MC

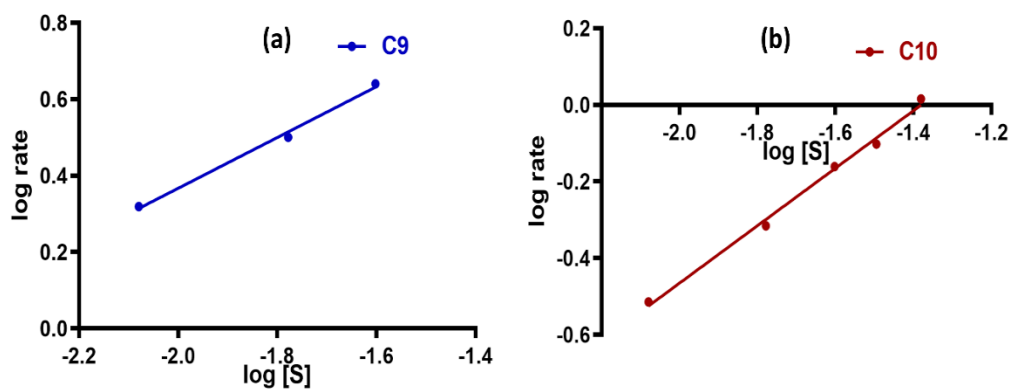


Fig. S4.20 Plot of log rate vs log [Sub] for complexes (a) C9 and (b) C10 for 4-MC

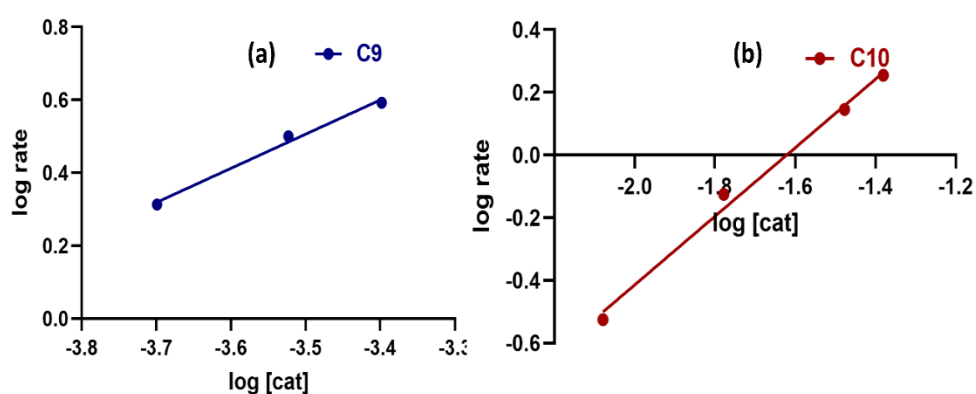


Fig. S4.21 Plot of log rate vs log [Cat] for complexes (a) C9 and (b) C10 for 4-MC

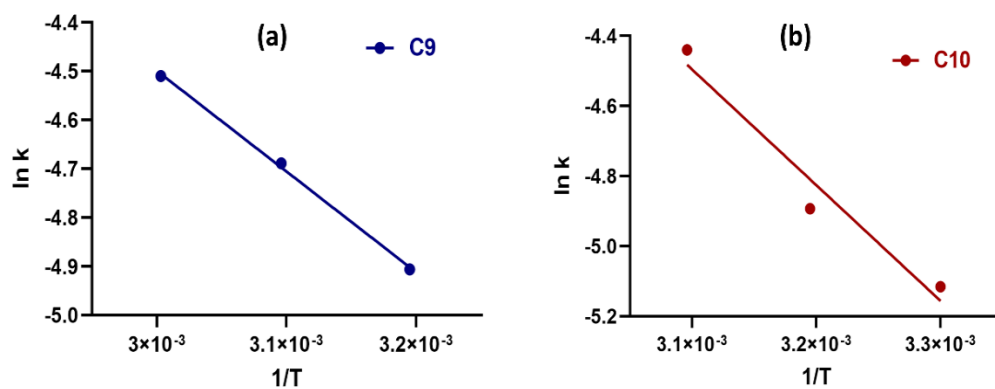
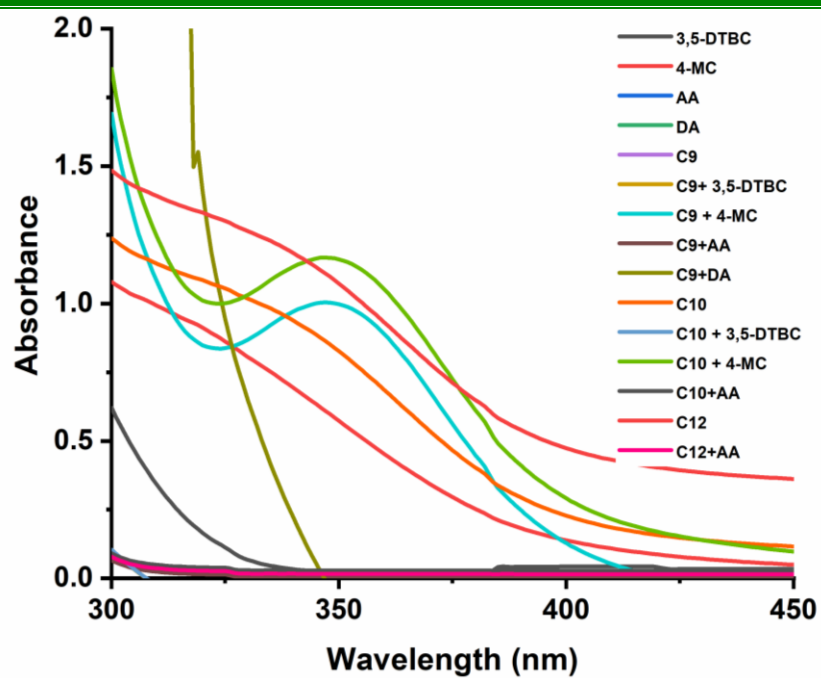


Fig. S4.22 Arrhenius plot of all complexes (a) C9 and (b) C10 for 4-MC



**Fig. S4.23** Electronic spectra of the formation of  $I_3^-$  ion in the presence of  $H_2O_2$  (detection was achieved as mentioned in the text).

---

**References**

1. Cheng, S.-C. & Wei, H.-H. Structure, magnetic properties and catecholase activity study of oxo-bridged dinuclear copper(II) complexes. *Inorganica Chim. Acta* **340**, 105–113 (2002).
2. Belle, C., Beguin, C., Gautier-Luneau, I., Hamman, S., Philouze, C., Pierre, J. L., Thomas, F., Torelli, S., Saint-Aman, E. & Bonin, M. Dicopper(II) Complexes of H-BPMP-Type Ligands: pH-Induced Changes of Redox, Spectroscopic ( $^{19}\text{F}$  NMR Studies of Fluorinated Complexes), Structural Properties, and Catecholase Activities. *Inorg. Chem.* **41**, 479–491 (2002).
3. Yernale, N. G. & Bennikallu Hire Mathada, M. Preparation of octahedral Cu(II), Co(II), Ni(II) and Zn(II) complexes derived from 8-formyl-7-hydroxy-4-methylcoumarin: Synthesis, characterization and biological study. *J. Mol. Struct.* **1220**, 128659 (2020).
4. Mukherjee, D., Nag, P., Shteinman, A. A., Vennapusa, S. R., Mandal, U. & Mitra, M. Catechol oxidation promoted by bridging phenoxo moieties in a bis( $\mu$ -phenoxo)-bridged dicopper(ii) complex. *RSC Adv.* **11**, 22951–22959 (2021).
5. Gentshev, P., Lüken, M., Möller, N., Rompel, A. & Krebs, B. Synthesis of a novel  $\mu$ -acetate bridged dinuclear Cu(II) complex as model compound for the active site of tyrosinase: crystal structure, magnetic properties and catecholase activity. *Inorg. Chem. Commun.* **4**, 753–756 (2001).
6. Kulkarni, A., Avaji, P. G., Bagihalli, G. B., Patil, S. A. & Badami, P. S. Synthesis, spectral, electrochemical and biological studies of Co(II), Ni(II) and Cu(II) complexes with Schiff bases of 8-formyl-7-hydroxy-4-methyl coumarin. *J. Coord. Chem.* **62**, 481–492 (2009).
7. Halli, M. B., Sumathi, R. B. & Kinni, M. Synthesis, spectroscopic characterization and biological evaluation studies of Schiff's base derived from naphthofuran-2-carbohydrazide with 8-formyl-7-hydroxy-4-methyl coumarin and its metal complexes. *Spectrochim. Acta Part A Mol. Biomol. Spectrosc.* **99**, 46–56 (2012).
8. Potapov, A. S., Nudnova, E. A., Domina, G. A., Kirpotina, L. N., Quinn, M. T., Khlebnikov, A. I. & Schepetkin, I. A. Synthesis, characterization and potent superoxide dismutase-like activity of novel bis(pyrazole)-2,2'-bipyridyl mixed ligand copper(II) complexes. *Dalt. Trans.* 4488–4498 (2009).
9. Patel, M. N., Gandhi, D. S. & Parmar, P. A. SOD mimic activity, DNA binding and in-vitro antibacterial studies of drug based copper(II) complexes. *Inorg. Chem. Commun.* **13**, 618–621 (2010).
10. Patel, M. N., Patel, C. R. & Joshi, H. N. Metal-based biologically active compounds: Synthesis, characterization, DNA interaction, antibacterial, cytotoxic and SOD mimic activities. *Appl. Biochem. Biotechnol.* **169**, 1329–1345 (2013).
11. Patel, M. N., Bhatt, B. S. & Dosi, P. A. Study of SOD mimic and nucleic acid interaction activity exerted by enrofloxacin-based copper(II) complexes. *Chem. Biodivers.* **9**, 2810–2824 (2012).
12. Dolomanov, O. V., Bourhis, L. J., Gildea, R. J., Howard, J. A. K. & Puschmann, H. OLEX2: A complete structure solution, refinement and analysis program. *J. Appl. Crystallogr.* **42**, 339–341 (2009).
13. Sheldrick, G. M. A short history of SHELX. *Acta Crystallogr. Sect. A Found. Crystallogr.* **64**, 112–122 (2008).
14. Sheldrick, G. M. Crystal structure refinement with SHELXL. *Acta Crystallogr. Sect. C* **71**, 3–8 (2015).

15. Frisch, M. J., Trucks, G. W., Schlegel, H. B., Scuseria, G. E., Robb, M. A., Cheeseman, J. R., Scalmani, G., Barone, V., Petersson, G. A., Nakatsuji, H., Li, X., Caricato, M., Marenich, A. V., Bloino, J., Janesko, B. G., Gomperts, R., Mennucci, B., Hratchian, H. P., Ortiz, J. V. *et al.* Gaussian 16, Revision A.03. *Gaussian, Inc., Wallingford CT* (2016).
16. Stephens, P. J., Devlin, F. J., Chabalowski, C. F. & Frisch, M. J. Ab Initio Calculation of Vibrational Absorption and Circular Dichroism Spectra Using Density Functional Force Fields. *J. Phys. Chem.* **98**, 11623–11627 (1994).
17. Hay, P. J. & Wadt, W. R. Ab initio effective core potentials for molecular calculations. Potentials for K to Au including the outermost core orbitals. *J. Chem. Phys.* **82**, 299–310 (1985).
18. Wadt, W. R. & Hay, P. J. Ab initio effective core potentials for molecular calculations. Potentials for main group elements Na to Bi. *J. Chem. Phys.* **82**, 284–298 (1985).
19. Dennington, R., Keith, T. A. & Millam, J. M. GaussView, Version 6. at (2016).
20. Lever, A. B. P. (Alfred B. P. *Inorganic electronic spectroscopy*, Elsevier, New York. (Elsevier Pub. Co, 1968).
21. Crawford, V. H., Richardson, H. W., Wasson, J. R., Hodgson, D. J. & Hatfield, W. E. Relation between the singlet-triplet splitting and the copper-oxygen-copper bridge angle in hydroxo-bridged copper dimers. *Inorg. Chem.* **15**, 2107–2110 (1976).
22. Gupta, R., Mukherjee, S. & Mukherjee, R. Synthesis, magnetism, <sup>1</sup>H NMR and redox activity of dicopper(II) complexes having a discrete {Cu<sub>2</sub>(μ-phenoxide)<sub>2</sub>}<sup>2+</sup> unit supported by a non-macrocyclic ligand environment. Crystal structure of [Cu<sub>2</sub>(L)<sub>2</sub>(OCIO<sub>3</sub>)<sub>2</sub>] [HL = 4-methyl-2,6-bis(pyrazol-1-ylmethyl)phen. *J. Chem. Soc. Dalt. Trans.* 4025–4030 (1999).
23. Saimiya, H., Sunatsuki, Y., Kojima, M., Kashino, S., Kambe, T., Hirotsu, M., Akashi, H., Nakajima, K. & Tokii, T. Antiferromagnetism induced by successive protonation of terminal phenol groups of a bis(μ-phenoxide)-bridged dicopper(II,II) complex. *J. Chem. Soc. Dalt. Trans.* 3737–3742 (2002).
24. Chattopadhyay, T., Banu, K. S., Banerjee, A., Ribas, J., Majee, A., Nethaji, M. & Das, D. A novel single pot synthesis of binuclear copper(II) complexes of macrocyclic and macroacyclic compartmental ligands: Structures and magnetic properties. *J. Mol. Struct.* **833**, 13–22 (2007).
25. Nag, K. Structure function relationship in some macrocyclic dicopper complexes. *Proc. Indian Acad. Sci. Chem. Sci.* **102**, 269–282 (1990).
26. Thirumavalavan, M., Akilan, P., Kandaswamy, M., Chinnakali, K., Kumar, G. S. & Fun, H. K. Synthesis of lateral macrobicyclic compartmental ligands: Structural, magnetic, electrochemical, and catalytic studies of mono- and binuclear copper(II) complexes. *Inorg. Chem.* **42**, 3308–3317 (2003).
27. Ruiz, E., Alemany, P., Alvarez, S. & Cano, J. Structural Modeling and Magneto-Structural Correlations for Hydroxo-Bridged Copper(II) Binuclear Complexes. *Inorg. Chem.* **36**, 3683–3688 (1997).
28. Ruiz, E., Alemany, P., Alvarez, S. & Cano, J. Toward the prediction of magnetic coupling in molecular systems: Hydroxo- and alkoxo-bridged Cu(II) binuclear complexes. *J. Am. Chem. Soc.* **119**, 1297–1303 (1997).
29. Shoba, D., Periandy, S., Karabacak, M. & Ramalingam, S. Vibrational spectroscopy (FT-IR and FT-Raman) investigation, and hybrid computational (HF and DFT) analysis on the structure of 2,3-naphthalenediol. *Spectrochim. Acta Part A Mol. Biomol. Spectrosc.* **83**, 540–552 (2011).
30. Fukui, K. Role of Frontier Orbitals in Chemical Reactions. *Science (80-. )*. **218**, 747–

- 754 (1982).
31. Wang, Q., Chen, D., Liu, X. & Zhang, L. Theoretical mechanisms of the superoxide radical anion catalyzed by the nickel superoxide dismutase. *Comput. Theor. Chem.* **966**, 357–363 (2011).
  32. Jawaria, R., Hussain, M., Khalid, M., Khan, M. U., Tahir, M. N., Naseer, M. M., Braga, A. A. C. & Shafiq, Z. Synthesis, crystal structure analysis, spectral characterization and nonlinear optical exploration of potent thiosemicarbazones based compounds: A DFT refine experimental study. *Inorganica Chim. Acta* **486**, 162–171 (2019).
  33. Koopmans, T. Über die Zuordnung von Wellenfunktionen und Eigenwerten zu den Einzelnen Elektronen Eines Atoms. *Physica* **1**, 104–113 (1934).
  34. Patel, R. N., Singh, N. & Gundla, V. L. N. Synthesis, characterization and superoxide dismutase activity of some octahedral nickel(II) complexes. *Polyhedron* **26**, 757–762 (2007).
  35. Patel, R. N. Synthesis, characterization and superoxide dismutase activity of some four coordinated copper(ii) complexes. *Indian J. Chem. - Sect. A Inorganic, Phys. Theor. Anal. Chem.* **48**, 1370–1377 (2009).
  36. Patel, R. N., Singh, N., Shukla, K. K. & Gundla, V. L. N. E.S.R., magnetic, electronic and superoxide dismutase studies of imidazolate-bridged Cu(II)-Cu(II) complexes with ethylenediamine as capping ligand. *Spectrochim. Acta - Part A Mol. Biomol. Spectrosc.* **61**, 1893–1897 (2005).
  37. He, S.-B., Hu, A.-L., Zhuang, Q.-Q., Peng, H.-P., Deng, H.-H., Chen, W. & Hong, G.-L. Ascorbate Oxidase Mimetic Activity of Copper(II) Oxide Nanoparticles. *ChemBioChem* **21**, 978–984 (2020).
  38. Liu, C., Cai, Y., Wang, J., Liu, X., Ren, H., Yan, L., Zhang, Y., Yang, S., Guo, J. & Liu, A. Facile Preparation of Homogeneous Copper Nanoclusters Exhibiting Excellent Tetraenzyme Mimetic Activities for Colorimetric Glutathione Sensing and Fluorimetric Ascorbic Acid Sensing. *ACS Appl. Mater. Interfaces* **12**, 42521–42530 (2020).
  39. Guo, D., Li, C., Liu, G., Luo, X. & Wu, F. Oxidase Mimetic Activity of a Metalloporphyrin-Containing Porous Organic Polymer and Its Applications for Colorimetric Detection of Both Ascorbic Acid and Glutathione. *ACS Sustain. Chem. Eng.* **9**, 5412–5421 (2021).
  40. Monzani, E., Battaini, G., Perotti, A., Casella, L., Gullotti, M., Santagostini, L., Nardin, G., Randaccio, L., Geremia, S., Zanello, P. & Opromolla, G. Mechanistic, structural, and spectroscopic studies on the catecholase activity of a dinuclear copper complex by dioxygen. *Inorg. Chem.* **38**, 5359–5369 (1999).
  41. Monzani, E., Quinti, L., Perotti, A., Casella, L., Gullotti, M., Randaccio, L., Geremia, S., Nardin, G., Faleschini, P. & Tabbì, G. Tyrosinase models. Synthesis, structure, catechol oxidase activity, and phenol monooxygenase activity of a dinuclear copper complex derived from a triamino pentabenzimidazole ligand. *Inorg. Chem.* **37**, 553–562 (1998).
  42. Ackermann, J., Meyer, F., Kaifer, E. & Pritzkow, H. Tuning the Activity of Catechol Oxidase Model Complexes by Geometric Changes of the Dicopper Core. *Chem. – A Eur. J.* **8**, 247–258 (2002).
  43. González-Álvarez, M., Alzuet, G., Borrás, J., García-Granda, S. & Montejo-Bernardo, J. M. Structural and functional models for the dinuclear copper active site in catechol oxidases: Synthesis, X-ray crystal structures, magnetic and spectroscopic properties of  $\mu$ -methoxo-bridged dinuclear copper(II) complexes with N-substituted sulfonamide ligand. *J. Inorg. Biochem.* **96**, 443–451 (2003).

44. Anbu, S. & Kandaswamy, M. Electrochemical, magnetic, catalytic, DNA binding and cleavage studies of new mono and binuclear copper(II) complexes. *Polyhedron* **30**, 123–131 (2011).
45. Tang, J., Luan, F. & Chen, X. Binding analysis of glycyrrhetic acid to human serum albumin: Fluorescence spectroscopy, FTIR, and molecular modeling. *Bioorganic Med. Chem.* **14**, 3210–3217 (2006).
46. Dutta, S., Mayans, J. & Ghosh, A. Facile synthesis of a new Cu(II) complex with an unsymmetrical ligand and its use as an O<sub>3</sub> donor metalloligand in the synthesis of Cu(II)-Mn(II) complexes: Structures, magnetic properties, and catalytic oxidase activities. *Dalt. Trans.* **49**, 1276–1291 (2020).

•